Atmos. Meas. Tech. Discuss., 7, 1393–1455, 2014
www.atmos-meas-tech-discuss.net/7/1393/2014/
doi:10.5194/amtd-7-1393-2014

Atmospheric Measurement Techniques Discussions

The performance of Aeolus in heterogeneous atmospheric conditions using high-resolution radiosonde data

X. J. Sun[1], R. W. Zhang[1], G. J. Marseille[2], A. Stoffelen[2], D. Donovan[3], L. Liu[1], and J. Zhao[1]

[1]College of Meteorology and Oceanography, PLA University of Science and Technology, Nanjing, China
[2]Weather Research Department of the Royal Netherlands Meteorological Institute, De Bilt, The Netherlands
[3]Regional Climate Department of the Royal Netherlands Meteorological Institute, De Bilt, The Netherlands

Received: 24 October 2013 – Accepted: 30 January 2014 – Published: 12 February 2014

Correspondence to: R. W. Zhang (weishen365@gmail.com)

Published by Copernicus Publications on behalf of the European Geosciences Union.

Abstract

The ESA Aeolus mission aims to measure wind profiles from space. In preparation for launch we aim to assess the expected bias in retrieved winds from the Mie and Rayleigh channel signals induced by atmospheric heterogeneity. Observation biases are known to be detrimental when gone undetected in Numerical Weather Prediction (NWP). Aeolus processing equipment should therefore be prepared to detect heterogeneous atmospheric scenes and take measures, e.g., reject or reduce the weight of observations when used in NWP.

Radiosondes provide the wind vector at about 10 m resolution. We present a method to simulate co-located cloud and aerosol optical properties from radiosonde observations. We show that cloud layers can be detected along the radiosonde path from radiosonde measured relative humidity and temperature. A parameterization for aerosol backscatter and extinction along the radiosonde path is presented based on a climatological aerosol backscatter profile and radiosonde relative humidity. The resulting high-resolution database of atmospheric wind and optical properties serves as input for Aeolus wind simulations.

It is shown that Aeolus wind error variance grows quadratically with bin size and the wind-shear over the bin. Strong scattering aerosol or cloud layers may cause biases exceeding 1 ms^{-1} for typical tropospheric conditions and 1 km Mie channel bin size, i.e., substantially larger than the mission bias requirement of 0.4 ms^{-1}. Advanced level-2 processing of Aeolus winds including estimation of atmosphere optical properties is needed to detect regions with large heterogeneity, potentially yielding biased winds.

Besides applicable for Aeolus the radiosonde database of co-located high-resolution wind and cloud information can be used for the validation of atmospheric motion wind vectors (AMV) or to correct their height assignment errors.

AMTD
7, 1393–1455, 2014

1 Introduction

The ESA Aeolus mission to measure wind profiles from space is scheduled for launch in the second half of 2015. Aeolus is a sun-synchronous dawn-dusk polar-orbiting satellite that carries a Doppler wind lidar with a fixed line-of-sight (LOS) pointing towards the atmosphere at 35° off-nadir and 90° across the satellite ground track on the earth surface, away from the sun. As such Aeolus measures a single LOS wind component rather than the complete wind vector. The lidar is operated in the ultraviolet (UV) part of the electromagnetic spectrum at 355 nm laser wavelength. At this wavelength, atmospheric scattering applies to both particles (aerosols, cloud droplets) and molecules. The combined spectrally broadened Rayleigh (molecular) signal and spectrally thin Mie (particle) signal are separated by the instrument receiver hardware (ESA, 2008), potentially yielding two wind solutions for the sampled volume, from the Mie and Rayleigh channel signals respectively.

The return signal from the atmosphere is divided in sequential time intervals that determine the vertical (range gate) resolution of the retrieved wind profile. The number of vertical bins is limited by instrument hardware to 24 for both the Mie and Rayleigh channels with minimum and maximum bin sizes of 250 m and 2000 m respectively. Intermediate bin sizes must be multiples of 250 m. The mission requirement for the horizontally projected line-of-sight (HLOS) (Marseille, 2003) wind error standard deviation of 1–2 ms^{-1} in the PBL, 2–3 ms^{-1} in the free troposphere and 3–5 ms^{-1} in the lower stratosphere is achieved for bin sizes of typically 250–500 m in the boundary layer, 1 km in the free troposphere and 2 km in the lower stratosphere. The maximum bin altitude is 32 km which is mainly driven by SNR considerations to yield Rayleigh channel winds that meet the mission requirement in the lower stratosphere.

ESA planned originally to operate the pulsed laser in burst mode (BM), in order to obtain rather independent and accurate wind profiles intermittently every 200 km, i.e., the instrument was switched on in cycles measuring for 7 s alternated by being switched off for 21 s (Stoffelen et al., 2005). In 2010 ESA decided to change to a continuous

AMTD
7, 1393–1455, 2014

pulsed-laser mode (CM). As a compromise and to meet the instrument energy budget, the laser pulse repetition frequency was decreased from 100 Hz to 50 Hz. As such, the amount of energy emitted into the atmosphere is about doubled when changing from BM to CM, which may be profitable.

The Aeolus CM sampling is characterized by a so-called basic repeat cycle (BRC) of 12 s, which translates to segments of about 86.4 km length along the satellite track for a satellite speed of about 7.2 $km\,s^{-1}$. The atmospheric signal scattered back to the instrument is collected and accumulated at 0.4 s intervals, i.e., corresponding to 20 shots or 2.88 km along track. These samples are denoted measurements. A BRC is thus composed of 30 measurements. These measurements are broadcasted to the ground segment for processing and wind retrieval (ESA, 2008). The processing for CM has been made flexible to combine measurements from adjacent BRCs.

In preparation for the Aeolus mission a number of activities have been conducted over more than a decade including the definition of atmospheric databases (Vaughan et al., 1998; Houchi et al., 2010; Marseille et al., 2011), instrument simulation (Marseille and Stoffelen, 2003), impact assessment for NWP (Stoffelen et al., 2006; Tan et al., 2007; Marseille et al., 2008) and the development of the ground segment processors (Tan et al., 2008a, b). The quality of Aeolus winds is largely determined by the (random) instrument noise and the variability of the atmospheric dynamics and optical properties within the sampling volume of typically 80–100 km along track and 1 km vertically. Atmospheric heterogeneity may cause substantial systematic errors in case of substantial wind-shear in combination with a heterogeneous distribution of particles inside the sampling volume. It is well-known that systematic errors are detrimental when used in NWP models and advanced quality control (QC) is needed to identify erroneous observations. The development of QC tools requires an atmospheric database at high resolution, i.e., substantially higher than the Aeolus sampling, to realistically simulate Aeolus performance in heterogeneous atmospheric scenes.

The “Holy grail” of a global database of both high resolution wind, temperature and atmosphere optical properties is not yet available and collocation data sets are

AMTD
7, 1393–1455, 2014

currently required to simulate Aeolus operation and wind profiles. The atmospheric database described in Marseille et al. (2011) is composed of atmospheric backscatter and extinction at 355 nm retrieved from CALIPSO attenuated backscatter at 532 nm and atmospheric dynamics and temperature from the ECMWF model interpolated to the CALIPSO track. The horizontal and vertical sampling of the database is 3.5 km and 125 m respectively. The effective resolution of the NWP dynamics and temperature components of the database are limited since it is well-known that NWP models do not well resolve atmospheric scales smaller than about 7 times the model grid size for mesoscale models (Skamarock, 2004). The ECMWF global model effective horizontal resolution is typically 15–20 times the model grid size in the free troposphere, i.e., about 375–500 km for the 2007 operational model version (Marseille et al., 2013) used in (Houchi et al., 2010). Houchi et al. (2010) showed that the 2007 ECMWF effective vertical model resolution is about 1.7 km, i.e., also substantially smaller than the spacing between the model levels. As a consequence, the model underestimates vertical wind shear of the horizontal wind by a factor of 2.5–3 on average relative to the shear as observed by radiosondes.

In this paper we discuss the heterogeneity of the atmosphere and its implications for the quality of Aeolus winds. The horizontal integration length is oversampled, i.e., typically 30 measurements are available for an integrated observation over 86 km. This provides information on the atmospheric heterogeneity along the track, e.g. large signal variations in turbulent regions, and the classification procedure of the Aeolus level-2 processor (Tan et al., 2008a, b) is used to apply QC and integrate these measurements in an optimal way. Generally, no oversampling is done in the vertical. The errors of retrieved winds resulting from an inhomogeneous distribution of particles within the measurement bin and varying wind with altitude has not been well quantified so far because of lacking datasets of combined wind and particle backscatter at high resolution, i.e., substantially higher than the Aeolus bin size of typically 250–2000 m in the vertical.

In this paper we focus on the vertical heterogeneity of the atmosphere and its implications for the quality of Aeolus winds. An analytical calculation is provided in Sect. 2.

AMTD
7, 1393–1455, 2014

These calculations are complemented by radiosonde data in the remainder of the paper. Radiosondes provide wind information and specific humidity at about 10 m resolution from the launch location up to about 30 km altitude (Houchi et al., 2010). Section 3 presents a method to detect cloud layers from radiosonde data launched in De Bilt. To complete the atmospheric backscatter profile, aerosol backscatter along the radiosonde path is simulated from a climatological aerosol backscatter profile and radiosonde humidity as discussed in Sect. 4. The simulated aerosol backscatter variability is validated against data from the UV lidar from the Cabauw observation site, close to De Bilt. The combined aerosol and cloud backscatter estimate is used as a proxy for the particle distribution along the radiosonde trajectory that is fed in the Aeolus simulation tool in Sect. 5 to estimate the wind error induced by atmospheric heterogeneity. Section 6 concludes with the summary and conclusions.

2 Impact of atmosphere heterogeneity on the quality of Aeolus winds

A single Aeolus wind observation corresponds to an atmospheric slice with dimensions of typically 50–100 km along track (horizontal) and / km in the vertical. Typical values for / range from 0.25–2. The along-track observation length is subdivided by typically 30 measurements, as described in Sect. 1. The Aeolus level-2 processor includes a classification module that provides representative weights to the measurements, based on the measured horizontal optical heterogeneity, before integration to an observation (Tan et al., 2008a, b). Since we have handles to control the along-track integration of the received atmospheric signal, it is expected that the wind error induced through atmospheric heterogeneity along the satellite track is small as compared to the atmospheric heterogeneity in the vertical that is generally not oversampled. Without additional information, e.g., from other instruments or models, we lack knowledge on the exact distribution of particles inside the measurement bin. The measured wind from particles or molecules inside the measurement bin, denoted $u_{\mathrm{p}}^{\mathrm{M}}$ and $u_{\mathrm{m}}^{\mathrm{M}}$ respectively, can in general be written as a weighted average, denoted by w, of the true wind u

AMTD
7, 1393–1455, 2014

inside the bin of length l as follows:

$$u_k^{\mathrm{M}} = \frac{\int_{z_0}^{z_l} w_k(z)u(z)\mathrm{d}z}{\int_{z_0}^{z_l} w_k(z)\mathrm{d}z}, \quad k = \{\mathrm{p},\mathrm{m}\} \tag{1}$$

with z denoting altitude and z_0 and z_l denoting the bottom and top altitude of the vertical bin respectively. The weight function w for the Mie channel is related directly to the attenuated particle backscatter, β'_{p}, inside the measurement bin and for the Rayleigh channel to the attenuated molecular backscatter, β'_{m}. These are defined as follows:

$$\begin{aligned} w_k(z) &= \beta'_k(z) \\ &= \beta_k(z)\tau^2(z) \\ &= \beta_k(z)\tau_{\mathrm{m}}^2(z)\tau_{\mathrm{p}}^2(z); \quad k = \{\mathrm{p},\mathrm{m}\} \end{aligned} \tag{2}$$

with $\tau(z)$ the total one-way atmospheric transmission of the laser light between the instrument and altitude z, above the earth surface, that decreases when penetrating deeper into the troposphere through particle and molecule backscatter and absorption. Particle and molecular transmission are denoted τ_{p}, and τ_{m} respectively. The weight function very much depends on the local atmosphere optical conditions: the distribution of aerosol and cloud particles, temperature and pressure. In the following subsections some special atmospheric situations are considered.

2.1 Infinitesimal thin particle layer

Consider a constant wind-shear with value α (s^{-1}) over the measurement bin. The wind velocity, u ($\mathrm{m\,s}^{-1}$), inside the bin of length l can thus be modelled through $u(z) = u_0 + \alpha z$, with u_0 the wind velocity at the bottom of the bin. The true mean wind inside the bin

AMTD
7, 1393–1455, 2014

thus equals $u^{\mathrm{T}} = u_0 + \alpha l/2$. Assume an infinitesimal thin particle (cloud or aerosol) layer inside the bin with unknown position. For an infinitesimal thin cloud layer the particle backscatter can be modelled with a delta-dirac function, δ, as follows: zero throughout the measurement bin and a spike with value β_{c} at the cloud layer location z_{c}: $\beta_{\mathrm{p}}(z) = \beta_{\mathrm{c}}\delta(z_{\mathrm{c}})$. The total cloud transmission is denoted τ_{c}, yielding for the particle transmission inside the bin: $\tau_{\mathrm{p}}(z) = 1$ for $z > z_{\mathrm{c}}$ and $\tau_{\mathrm{p}}(z) = \tau_{\mathrm{c}}$ for $z \le z_{\mathrm{c}}$.

From Eq. (2) we have for the Mie channel $w_{\mathrm{p}}(z) = \beta_{\mathrm{c}}\delta(z_{\mathrm{c}})\tau_{\mathrm{c}}^2\tau_{\mathrm{m}}^2(z_{\mathrm{c}})$ for $z = z_{\mathrm{c}}$ and $w_{\mathrm{p}}(z) = 0$ otherwise. Substituting in Eq. (1) yields $u_{\mathrm{p}}^{\mathrm{M}} = u_0 + \alpha z_{\mathrm{c}}$, i.e., the wind velocity at the location of the particle layer. The location of the cloud inside the bin is not known and it can not be determined from the measured Aeolus Mie signal. The cloud location has equal probability for all locations inside the measurement bin and can thus be modelled through a uniform probability density function with amplitude l^{-1}. The expectation value, μ, and variance, σ^2, of the cloud location z_{c} are then easily derived:

$$\mu_{z_{\mathrm{c}}} = l/2; \quad \sigma^2_{z_{\mathrm{c}}} = l^2/12 \tag{3}$$

For the wind velocity error, $\varepsilon(z_{\mathrm{c}})$, of the measured wind we may write

$$\varepsilon_k(z_{\mathrm{c}}) = u_k^{\mathrm{M}} - u^{\mathrm{T}} \tag{4}$$

which equals $\alpha(z_{\mathrm{c}} - l/2)$ when substituting the corresponding values derived above for the Mie channel wind ($k = \mathrm{p}$). From Eq. (3) the expectation value and variance of $\varepsilon_{\mathrm{p}}(z_{\mathrm{c}})$ equal

$$\mu_{\varepsilon_{\mathrm{p}}(z_{\mathrm{c}})} = 0 \tag{5}$$

$$\sigma^2_{\varepsilon_{\mathrm{p}}(z_{\mathrm{c}})} = \alpha^2 l^2/12 \tag{6}$$

respectively, i.e., the Aeolus Mie channel wind velocity error variance grows quadratically with increasing bin size and increasing wind shear over the bin.

AMTD
7, 1393–1455, 2014

For the Rayleigh channel the weight function is also determined by the total attenuated backscatter inside the measurement bin. For simplicity we ignore the altitude dependence of the attenuated molecular backscatter inside the bin (see Eq. 2) and assume a constant attenuated molecular backscatter inside the measurement bin: $\beta_m(z)\tau_m^2(z) = w_0$. The weight function inside the bin, $w_m(z)$, then equals w_0 for $z_c \le z < z_l$ and $\tau_c^2 w_0$ for $z_0 \le z < z_c$. The wind velocity estimate from the Rayleigh channel signal then equals

$$
\begin{aligned}
u_m^M(z) &= u_0 + \frac{\int_{z_c}^{z_l} w_0 \alpha z \mathrm{d}z + \int_{z_0}^{z_c} \tau_c^2 w_0 \alpha z \mathrm{d}z}{\int_{z_c}^{z_l} w_0 \mathrm{d}z + \int_{z_0}^{z_c} \tau_c^2 w_0 \mathrm{d}z} \\
&= u_0 + \frac{\alpha}{2} \frac{\left(1-\tau_c^2\right)\left(z_0^2 - z_c^2\right) + \left(z_l^2 - z_0^2\right)}{\left(1-\tau_c^2\right)(z_0 - z_c) + (z_l - z_0)} \\
&= u_0 + \frac{\alpha}{2} \frac{\left(\tau_c^2 - 1\right) z_c^2 + l^2}{\left(\tau_c^2 - 1\right) z_c + l}
\end{aligned}
\tag{7}
$$

where we used $z_0 = 0$ and $z_l = l$ in the last step for convenience in the remainder of the calculations. Substituting Eq. (7) in Eq. (4) with $k = \mathrm{m}$ yields for the Rayleigh channel wind velocity error

$$
\varepsilon_m(z_c) = \frac{\alpha}{2}\left[\frac{\left(\tau_c^2 - 1\right) z_c^2 + l^2}{\left(\tau_c^2 - 1\right) z_c + l} - l\right] \tag{8}
$$

AMTD
7, 1393–1455, 2014

A first order Taylor expansion for $\varepsilon_{\mathrm{m}}(z_{\mathrm{c}})$ yields

$$\varepsilon_{\mathrm{m}}(z_{\mathrm{c}}) \approx \varepsilon_{\mathrm{m}}\left(\mu_{z_{\mathrm{c}}}\right) + \frac{\partial \varepsilon}{\partial z}\left(\mu_{z_{\mathrm{c}}}\right)\left[z_{\mathrm{c}} - \mu_{z_{\mathrm{c}}}\right] \tag{9}$$

The expectation value of ε then follows from Eqs. (3), (8), and (9):

$$\begin{aligned}\mu_{\varepsilon_{\mathrm{m}}(z_{\mathrm{c}})} &= E\left[\varepsilon_{\mathrm{m}}(z_{\mathrm{c}})\right] = \varepsilon_{\mathrm{m}}\left(\mu_{z_{\mathrm{c}}}\right) \\ &= \frac{\alpha}{2}\left[\frac{\left(\tau_{\mathrm{c}}^2 - 1\right)(l/2)^2 + l^2}{\left(\tau_{\mathrm{c}}^2 - 1\right)(l/2) + l} - l\right] \\ &= \frac{\alpha l}{2}\left[\frac{\tau_{\mathrm{c}}^2 + 3}{2\left(1 + \tau_{\mathrm{c}}^2\right)} - 1\right]\end{aligned} \tag{10}$$

with E the expectation operator. From Eq. (10) it follows that the Rayleigh channel wind velocity bias grows linearly with increasing bin size and increasing wind shear inside the bin and quadratic with the cloud layer transmission. For optically very thin clouds with a transmission value close to 1, the wind velocity bias is close to zero, as expected. Worst case scenario for Rayleigh channel wind errors is an opaque cloud with transmission 0. From Eq. (10) the mean bias has a value of $\alpha l/4$, in agreement with a maximum bias of $\alpha l/2$ when the cloud is located at the top of the bin and the minimum bias of 0 when the cloud is located at the bottom of the bin. For a typical wind shear in the free troposphere of $0.004\,\mathrm{s}^{-1}$ and an Aeolus bin size of 1 km, the mean bias of Rayleigh channel winds for an opaque clouds is $1\,\mathrm{ms}^{-1}$, i.e., exceeding the mission requirement of $0.4\,\mathrm{ms}^{-1}$ (ESA, 2008). This result motivates the classification procedure implemented in the level-2 processor to select measurements that are free of particles before integrating the measurements to observation level.

AMTD
7, 1393–1455, 2014

For a cirrus cloud in the tropics with a typical transmission value of 0.9 and an Aeolus bin size of 1 km the situation is with a mean wind bias of 0.1 ms^{-1} less dramatic, i.e., well within the Aeolus bias requirement of 0.4 ms^{-1}.

The Rayleigh wind error variance follows from Eq. (9):

$$\sigma^2_{\varepsilon_m(z_c)} = E\left[(\varepsilon_m(z_c) - \mu_{\varepsilon_m(z_c)})^2\right] = \left[\frac{\partial \varepsilon}{\partial z}(\mu_{z_c})\right]^2 E\left[(z_c - E(z_c))^2\right]$$
$$= \left[\frac{\left(\tau_c^2 - 1\right)}{\left(\tau_c^2 + 1\right)}\right]^2 \frac{\alpha^2 l^2}{48} \quad (11)$$

and using Eqs. (3) and (8). For a fully transparent cloud with τ_c equal to 1 the Rayleigh wind error equals zero and thus also its mean variance, which is clear from Eq. (11). For an opaque cloud with τ_c equal to 0, the mean variance of the Rayleigh wind error from Eq. (11) equals $\alpha^2 l^2/48$, i.e., the mean wind error variance grows quadratic with both the wind shear and bin size. Some numerical results are presented in Table 1.

Note that the extreme situation of τ_c equal to 1 is equivalent to a fully transparent cloud with no extinction and thus zero cloud backscatter when assuming a cloud lidar ratio value larger than 0. Then the Mie channel weight function equals 0 from Eq. (2). In other words Eq. (1) has no solution which is consistent for a particle-free measurement bin.

2.2 Thick cloud layer

In this section we generalize the procedure of the previous section by assuming the more realistic situation of a cloud layer of thickness $\delta z \neq 0$. The cloud layer is assumed symmetric with centre location at z_c. From Eq. (2) the Mie channel weight function then equals 0 for $z_0 \leq z < z_c - \delta z/2$, $\beta'_p(z)$ for $z_c - \delta z/2 \leq z \leq z_c + \delta z/2$ and 0 for $z > z_c + \delta z/2$. We assume $\beta'_p(z)$ constant with altitude for simplicity. Substituting in Eq. (1)

AMTD
7, 1393–1455, 2014

yields $u_p^M = u_0 + \alpha z_c$, similar as for the very thin cloud layer in the previous section. Again, the location of the cloud layer can be modelled as a uniform distribution but is limited to the interval $[z_0 - \delta z/2,\ l - \delta z/2]$. The amplitude of the uniform distribution is thus $(l - \delta z)^{-1}$. For the expectation value and variance of z_c we get

$$\mu_{z_c} = l/2; \quad \sigma_{z_c}^2 = (l - \delta z)^2/12 \tag{12}$$

From Eq. (4) the mean wind error of the measured Mie channel wind again equals $\varepsilon_p(z_c) = \alpha(z_c - l/2)$ with expectation value 0 and variance $\alpha^2(l - \delta z)^2/12$, i.e., smaller than for an infinitesimal thin cloud. The extreme value of δz equal to zero yields the same result as in the previous section, for δz equal to l, the mean Mie wind error variance equals zero which is consistent with a uniform weight function (attenuated backscattering) over the complete measurement bin.

For the Rayleigh channel wind we assume a linear weight function (cloud transmission) in the cloud layer. Again, the total one-way cloud transmission is denoted τ_c. The Rayleigh channel weight function then equals w_0 for $z > z_c + \delta z/2$, $az + b$ for $z_c - \delta z/2 \le z \le z_c + \delta z/2$ and $\tau_c^2 w_0$ for $z_0 \le z < z_c - \delta z/2$ with $a = w_0(1 - \tau_c^2)/\delta z$ and $b = w_0 - a(z_c + \delta z/2)$. Substituting in Eq. (2) yields for the measured Rayleigh wind

$$u_m^M(z) = \frac{\alpha}{2} \frac{\left(\tau_c^2 - 1\right) z_c^2 + \left(\tau_c^2 - 1\right) \delta z^2/12 + l^2}{\left(\tau_c^2 - 1\right) z_c + l} \tag{13}$$

i.e., similar to Eq. (7) but with an additional term in the numerator. For the Rayleigh wind error we get

$$\varepsilon_m(z_c) = \frac{\alpha}{2} \left[\frac{\left(\tau_c^2 - 1\right) z_c^2 + \left(\tau_c^2 - 1\right) \delta z^2/12 + l^2}{\left(\tau_c^2 - 1\right) z_c + l} - l \right] \tag{14}$$

AMTD
7, 1393–1455, 2014

This yields for the expectation value of the Rayleigh channel wind velocity error:

$$\mu_{\varepsilon_m(z_c)} = \frac{\alpha l}{2}\left[\frac{\tau_c^2+3}{2\left(1+\tau_c^2\right)} + \frac{\left(\tau_c^2-1\right)\delta z^2}{6l^2\left(1+\tau_c^2\right)} - 1\right] \quad (15)$$

i.e., the bias is smaller than for the infinitesimal thin cloud of the previous section, as expected. For the Rayleigh wind error variance we get

$$\sigma^2_{\varepsilon_m(z_c)} = \left[1-\left(\frac{\delta z}{l\sqrt{3}}\right)^2\right]\left[\frac{\left(\tau_c^2-1\right)}{\left(\tau_c^2+1\right)}\right]^2 \frac{\alpha^2 l^2}{48} \quad (16)$$

that is smaller than the variance for the infinitesimal thin cloud of the previous section, see Eq. (11). From Eqs. (15) and (16) it is clear that wind biases only occur in case that both the wind velocity and particle density vary with height inside the measurement bin, i.e., both $\alpha \neq 0$ and $\tau_c \neq 1$.

Figure 1 shows that the maximum bias value for Rayleigh winds is obtained for optically thick and geophysical thin particle layers. The actual value of the bias depends on the location of the layer inside the measurement bin, which is unknown without additional information. If such a layer is located at the bottom of the measurement bin, the error of the retrieved wind equals zero. On the other hand, the error has a maximum value of $2\,\mathrm{ms}^{-1}$ when the layer is located at the top of the measurement bin, when assuming a $0.004\,\mathrm{s}^{-1}$ wind shear over the 1 km. On average the wind velocity error (bias) equals $1\,\mathrm{ms}^{-1}$ (bottom left part of left panel in Fig. 1) in agreement with Table 1. The wind error variance (stand deviation) has a maximum value of $0.33\,\mathrm{m}^2\,\mathrm{s}^{-2}$ ($0.57\,\mathrm{m\,s}^{-1}$) (bottom left part of right panel in Fig. 1) in agreement with Table 1. For a particle layer covering half the bin and with transmission 0.5 the bias and standard deviation are $0.55\,\mathrm{ms}^{-1}$ and $0.33\,\mathrm{ms}^{-1}$ respectively. The black solid line in the left panel of Fig. 1 marks the Aeolus mission requirement of $0.4\,\mathrm{ms}^{-1}$ for the wind error bias. Rayleigh

AMTD
7, 1393–1455, 2014

winds that fulfil this mission requirement can be obtained, on average, from measurement bins with particle layers and one-way transmission exceeding 0.65. For geometrically thicker layers this constraint can be relaxed to transmission values up to 0.5, depending on layer thickness. These numbers are based on 0.004 s^{-1} wind shear over a 1 km measurement bin. Equations (15) and (16) may be used for other parameter values.

In the subsequent sections we complement to these analytical results by using real atmospheric winds and atmospheric backscatter derived from radiosonde data.

3 Estimation of cloud and aerosol backscatter and extinction from radiosonde data

Radiosonde data have been used to retrieve the cloud vertical structure and to estimate aerosol backscatter along the radiosonde path, mainly by utilizing the humidity parameter. In this study we use data from the radiosonde from the Dutch Meteorological Institute, KNMI, located in De Bilt, the Netherlands (52.1007° N, 5.1774° E, and 5 m a.s.l.). KNMI operates a Vaisala RS92 radiosonde that measures data every 2 s. With an average ascent rate of about 5 m s^{-1}, wind, temperature and humidity data are obtained at high vertical resolution of about 10 m. WMO intercomparison test results showed that the radiosonde RS92 is of high quality for all measurement parameters for in-situ monitoring of upper air conditions (Vaisala, 2011). During the entire study period, 1 January to 31 December 2007, radiosondes were launched 2 times a day (at 00:00 and 12:00 UTC) without any major interruption. Only the 12:00 UTC data were used in this study covering 310 valid launches of which 87.42 % reached altitudes exceeding 20 km. No data is available for the remaining 55 launches. The radiosondes collected profiles of temperature, relative humidity (RH), pressure, wind speed and direction.

AMTD
7, 1393–1455, 2014

3.1 Detection of cloud vertical structure

Radiosonde data can be used to retrieve the cloud vertical structure along the radiosonde path, mainly by utilizing the humidity parameter. Data quality and the calculation method determine the result to a large extent. Three methods that have been reported in literature include the dewpoint temperature depression method (Poore et al., 1995), the second derivative method (Chernykh and Eskridge, 1996), hereafter CE, and the relative humidity threshold method (Wang and Rossow, 1995), hereafter WR95. These methods are shortly summarized below.

In Poore's method, radiosonde observations are employed to determine the locations of cloud-layer top and base by testing for dewpoint temperature depressions below some threshold value. The vertical profile of dewpoint depression ΔT_d (i.e., the difference between temperature and dewpoint temperature) indicates possible moist layers if values drop below a threshold value. Used threshold values for ΔT_d are: 2 °C for temperatures above 0 °C, 4 °C for temperatures between 0 and −20 °C, and 6 °C for temperatures below −20 °C.

The CE method, on the other hand, determines cloud boundaries and cloud amounts from vertical profiles of temperature, RH, and dewpoint depression. First, cloud layers are detected by testing on $0 \leq T''(z)$ and $R''(z) \leq 0$, with T'' the second derivative of the vertical profile of temperature, R'' the second derivative of relative humidity and z denoting altitude. Next, if a cloud layer is detected, the dew point depression method of Poore, described above, is used to determine the cloud location.

WR95 is an improvement of Poore's method. WR95 determines the cloud vertical structure from RH profiles by using the same minimum and maximum RH thresholds of 84 % and 87 %, respectively, for all altitudes. Because WR95 uses a single RH threshold definition for all temperature values, it can determine the cloud vertical structure continuously, avoiding discontinuities at the boundaries of the temperature intervals of Poore's method. Also, one of the cloud formation conditions is that relative humidity tends to saturation; therefore, it is reasonable that the RH value is used directly as

AMTD
7, 1393–1455, 2014

a threshold value for cloud detection. The RH profile is examined from the surface to the top to find cloud layers in five steps: Eq. (1) the base of the lowest moist layer is determined as the level that satisfies any one of the three conditions: (a) minimum RH at least 87 %, (b) minimum RH at least 84 % if this level is the surface level, or (c) if this level is not the surface level, RH at least 84 % but less than 87 %, and RH increases at least 3 % from the adjacent lower level; Eq. (2) RH of the next levels above the layer base is at least 84 %, they are considered as being inside the moist layer; Eq. (3) the top of the moist layer is detected as the level that meets any one of the three conditions: (a) minimum RH at least 87 %, (b) minimum RH at least 84 % if this level is the top of the profile, or (c) if this level is not the top of the profile, RH at least 84 % but less than 87 %, and RH increases at least 3 % from the higher level; Eq. (4) the moist layer is classified as a cloud layer if the maximum RH within the moist layer is more than 87 %; and Eq. (5) the minimum cloud height is set to 500 m a.g.l. For "single level" clouds having the same level identified as top and base, cloud layer top is assigned as half the distance to the next level above and the base is at half the distance to the next level below.

In WR95, the condition that RH jumps over 3 % from one level to the next at the cloud base and top is easily satisfied, because the method developed in WR95 was based on radiosonde data at a relative low vertical resolution of about 200 m. However, this condition is much more difficult to meet for RS92 with much higher vertical resolution of about 10 m. Therefore, Zhang et al. (2010), hereafter Zhang2010, modified the WR95 method when applied to the analysis of cloud vertical structure using high-resolution radiosonde observations over the Shouxian region.

Zhang2010 is based on the method of WR95 with some modification for application to RS92 data. Most important, the RH of RS92 is given with respect to liquid water, RH_w, only and needs recalculation for all levels with temperatures below 0 °C to get RH with respect to ice: RH_i. Hereto we use the relations proposed by Alduchov and Eskridge (1996), which are summarized here. Based on the known radiosonde RH_w,

AMTD
7, 1393–1455, 2014

water vapor pressure, $e(T)$, is derived from:

$$e(T) = \mathrm{RH}_w \cdot e_w(T)/100 \quad (17)$$

with $e_w(T)$ the saturation vapor pressure over water (0–50 °C) that is defined as a function of temperature T (°C) from:

$$e_w(T) = 6.1094 \times e^{17.625T/(243.04+T)} \quad (18)$$

Therefore, RH_i with respect to ice (temperatures below 0 °C) is calculated from:

$$\mathrm{RH}_i = e(T)/e_i(T) \cdot 100 \quad (19)$$

with $e_i(T)$ is the saturation vapor pressure over a plane surface of ice (−80–0 °C) that is defined as a function of temperature T from:

$$e_i(T) = 6.1121 \times e^{22.587T/(273.86+T)} \quad (20)$$

The co-existence of liquid and ice is not considered in this method, and the results of the application of this method to radiosonde data of De Bilt are presented in Fig. 2. For the selected period, 271 launches reached altitudes exceeding 20 km. From these the levels are selected which are closest to the 60 ECMWF models levels, as such yielding a total of 60 × 271 samples. Figure 2 shows scatterplots of RH from the radiosonde vs. RH from the 2007 operational ECMWF model interpolated to the radiosonde launch location. Introducing the recalculation following the equations above, for a fair comparison including both water and ice phases, increases the correlation value from 0.826 to 0.890. RH values exceeding 100 % in Fig. 2 correspond to water vapor over-saturation of the air. The recalculated RH, giving RH with respect to water and ice, has been used as input to detect cloud layers from the radiosonde data.

The minimum RH thresholds (hereafter min-RH), the minimum RH within the distance between two contiguous layers (hereafter inter-RH) and maximum RH thresholds

AMTD
7, 1393–1455, 2014

(hereafter max-RH) are used to determine the cloud layer in Zhang2010 method. Table 2, obtained from Zhang2010, specifies the height-dependent threshold of max-RH, min-RH, and inter-RH values, also displayed in the right panel of Fig. 3.

The modified cloud detection algorithm in Zhang2010 is summarized as follows: (1) the base of the lowest moist layer is detected as the level when RH exceeds the min-RH corresponding to this level, see Table 2; (2) the next levels above the base are checked and are temporarily treated as the same layer when RH exceeds the value of the corresponding min-RH; (3) the top of the moist layer is determined when RH decreases to below the corresponding min-RH value or RH still exceeds the corresponding min-RH value but the top of the profile is reached; (4) moist layers with bases lower than 120 m and thicknesses less than 400 m are discarded; (5) the detected moist layer is finally classified as a cloud layer only if the maximum value of RH within this layer is larger than the corresponding value for max-RH; (6) the base of cloud layers is set to 280 m a.g.l., and cloud layers are discarded if their tops are lower than 280 m; (7) two contiguous layers are considered as a one-layer cloud if the distance between these two layers is less than 300 m or the minimum RH within this distance is more than the maximum inter-RH value within this distance; and (8) detected clouds are discarded for low-level clouds (below 2000 m) with thickness less than 30.5 m and for clouds above 2000 m with thickness less than 61 m.

Here we note that the Zhang2010 method described above was tuned for the Shouxian area during the rain season showing many days with fog layers near the surface. The climatological conditions for the Netherlands are quite different: there is no well-defined rain season and fog is a rare event. We therefore discard points (4) and (6) of the procedure described above to allow for the detection of cloud layers near the surface. In addition for point (7), when combining two contiguous layers into one-layer cloud, the distance between these two layers is increased to 500 m. This modification allows for validation with CloudSat/CALIPSO.

In the remainder of this study, we adopt the Zhang2010 method with the above modifications to detect cloud vertical structure over the Netherlands from radiosondes

AMTD
7, 1393–1455, 2014

launched at the Dutch meteorological weather institute in De Bilt. Analysis and results of cloud layer detection from radiosondes are discussed in Sect. 4.1.

3.2 Estimation of aerosol backscatter and extinction

Aerosols play an important role in climate change and have important consequences on the earth's radiation budget (Covert et al., 1979; IPCC, 2012). Water is an important solvent for constituents of atmospheric aerosol particles. As such, the optical properties of aerosol vary with the changing ambient relative humidity. Different types of aerosols respond differently to changing RH, ranging from a hydrophobic behaviour to a hygroscopic one (Randriamiarisoa et al., 2006). As a consequence, penetration of the Aeolus laser beam signal in the lower part of the atmosphere depends to a large extent on aerosol extinction and thus on aerosol type and RH (Boucher and Anderson, 1995).

The previous section discussed the detection of cloud layers over De Bilt. To complete the profile of scattering particles requires knowledge of the aerosol density and type over De Bilt. However, aerosol measurements are not performed in De Bilt. Instead we adopt the climatological aerosol backscatter profile at 355 nm, $\beta_{\mathrm{A}}^{\mathrm{clim}}(z)$ ($\mathrm{m}^{-1}\,\mathrm{sr}^{-1}$), that was derived from lidar flight campaigns over the Northern and Southern Atlantic in 1989 (Vaughan, 1998). The climatological aerosol backscatter profile has been used in many Aeolus studies and is also denoted the reference model atmosphere (RMA), see e.g. Marseille et al. (2011). This climatological profile is smooth and shows a strong decrease of aerosol density from the surface up to 5 km altitude, followed by a less strong decrease in the range 5–15 km, followed by a strong drop above 15 km. Here, we aim to generate a more realistic aerosol profile above De Bilt by adapting the climatological profile based on the relative humidity over De Bilt from radiosonde measurements and assuming a hygroscopic growth factor. The focus of this study is on the atmospheric heterogeneity with altitude and we assume a constant horizontal distribution of particles along a BRC.

AMTD
7, 1393–1455, 2014

Kasten (1969) studied the hygroscopic properties of aerosols, resulting in an empirical relation between the RH dependent aerosol scattering cross-section, $\sigma_{\text{scatt}}(\text{RH})$ (m^2) and an aerosol hygroscopic exponent γ:

$$\sigma_{\text{scatt}}(\text{RH}) = k \cdot (1 - \text{RH})^{-\gamma} \tag{21}$$

for a constant parameter k. The exponent γ depends on the hygroscopic nature of aerosols and it has been shown to vary for ambient aerosols according to their chemical composition (Hänel, 1976). Moreover, Hänel (1976) proposed a parameterization for the aerosol scattering growth factor $f_{\text{scatt}}(\text{RH})$ as a function of RH to address the hygroscopic effect of aerosol scattering. The growth factor $\sigma_{\text{scatt}}(\text{RH})$ is defined as the ratio between wet and dry scattering cross sections:

$$f_{\text{scatt}}(\text{RH}) = \sigma_{\text{scatt}}(\text{RH}) / \sigma_{\text{scatt, dry}} \tag{22}$$

with $\sigma_{\text{scatt, dry}}$ the scattering cross-section considering a "dry" RH over the range 20–40 % (Kotchenruther et al., 1999; Malm et al., 2003; Pan et al., 2009). After Hänel proposed the parameterization of $f_{\text{scatt}}(\text{RH})$, it has been used by many authors, and the $f_{\text{scatt}}(\text{RH})$ value at RH = 80 % is frequently used to appreciate the degree of hygroscopicity of aerosols in current literature (Ross et al., 1998; Kotchenruther et al., 1999; Gasso et al., 2000; Pan et al., 2009). Some authors (Randriamiarisoa et al., 2006; Sivakumar et al., 2009; Lin et al., 2013) used a different reference value $\sigma_{\text{scatt, ref}}$ corresponding to a reference RH value, RH = RH_{ref}, instead of the dry value $\sigma_{\text{scatt, dry}}$. Eq. (22) then becomes:

$$f_{\text{scatt}}(\text{RH}) = \left[(1 - \text{RH})/(1 - \text{RH}_{\text{ref}})\right]^{-\gamma}. \tag{23}$$

The hygroscopic growth factor for tropospheric aerosols has been discussed extensively in literature and defined as the ratio of the light scattering coefficient by an aerosol at 80 % RH to that at reference low 30 % RH (Hegg et al., 1993; Tang, 1996). A value of the hygroscopic growth factor 2.1 has been estimated by using 355 nm Raman lidar data in the Atmospheric Lidar EXperiment (ALEX) (Rogers et al., 2006),

AMTD
7, 1393–1455, 2014

which is slightly higher than Charlson's value of 1.7 normalized to 50 % RH (Charlson et al., 1991). Based on Eq. (23), the hygroscopic exponent, γ recalculated as 0.5922 by using the Rogers's value, is in agreement with Gasso et al. (2000). Moreover, the value of $f_{\mathrm{scatt}}(80\,\%)/f_{\mathrm{scatt}}(50\,\%)$ is 1.72, in agreement with the value reported by Charlson et al. (1991). For the present study, the above value for γ is considered applicable for average conditions over De Bilt, the Netherlands. From Eq. (23) the altitude dependent aerosol scattering growth factor becomes:

$$f_{\mathrm{scatt}}(\mathrm{RH}(z)) = [(1 - \mathrm{RH}(z)/100)/(1 - 30/100)]^{-0.5922} \tag{24}$$

Aerosol backscatter, $\beta_{\mathrm{A}}(z)$ ($\mathrm{m}^{-1}\,\mathrm{sr}^{-1}$), is then estimated from adapting the climatological aerosol backscatter profile:

$$\beta_{\mathrm{A}}(z) = \beta_{\mathrm{A}}^{\mathrm{clim}}(z) \cdot f_{\mathrm{scatt}}(\mathrm{RH}(z)). \tag{25}$$

Finally, aerosol extinction (m^{-1}) must be determined to estimate the laser beam transmission through the atmosphere. Many studies use a linear relationship between the aerosol backscatter and extinction coefficients (e.g., Evans, 1988; Spinhirne et al., 1997; Liu et al., 2002; Marseille et al., 2011).:

$$\frac{\alpha_{\mathrm{A}}}{\beta_{\mathrm{A}}} = S, \tag{26}$$

with α_{A} the aerosol extinction coefficient (m^{-1}), β_{A} the aerosol backscatter coefficient ($\mathrm{m}^{-1}\,\mathrm{sr}^{-1}$), and S is the extinction-to-backscatter ratio (sr) (also called the lidar ratio). Values for S vary over a large range depending on the wavelength of the incident light, the aerosol refractive index, and the aerosol size distribution (Ackermann, 1998). Moreover, these aerosol characteristics change with the ambient relative humidity. Experimental results show that the lidar ratio changes from 19.5 sr to 84 sr within the planetary boundary layer (PBL) depending on RH and laser wavelength (Waggoner et al., 1972; Salemink et al., 1984; Rosen et al., 1997). Ackermann (1998) proposed

AMTD
7, 1393–1455, 2014

a parameterization of the lidar ratio, $S(\mathrm{RH})$, as a power serious expansion of atmosphere RH:

$$S(\mathrm{RH}) \approx \sum_{j=1}^{J} a_j (\mathrm{RH})^{j-1}, \tag{27}$$

with a_j parameters that depend on laser wavelength and aerosol type. De Bilt is close to the coastal region but given the location of the four largest cities in the Netherlands close to the coast also human activity is concentrated west of De Bilt. The prevailing westerly winds over the Netherlands transport a mixture of marine and urban (also denoted pollution or continental) aerosol over De Bilt. Lidar measurements from the Cabauw site, further discussed in Sect. 4.2.2, identified urban aerosol as the dominant aerosol type over De Bilt. The corresponding parameters in the series expansion, Eq. (27), are obtained from Table 3 of Ackermann (1998) for continental aerosol: $J = 10$, $a_1 = 4.252 \times 10^{1}$, $a_2 = 4.400 \times 10^{-1}$, $a_3 = -7.877 \times 10^{-3}$, $a_4 = 1.395 \times 10^{-5}$, $a_5 = 7.881 \times 10^{-6}$, $a_6 = -1.472 \times 10^{-7}$, $a_7 = 8.581 \times 10^{-12}$, $a_8 = 1.350 \times 10^{-11}$, $a_9 = -2.899 \times 10^{-14}$, $a_{10} = -3.411 \times 10^{-16}$. From Eq. (26) we get for the estimated aerosol extinction coefficient:

$$\alpha_{\mathrm{A}}(z) = S(\mathrm{RH}(z)) \cdot \beta_{\mathrm{A}}(z), \tag{28}$$

with $\beta_{\mathrm{A}}(z)$ from Eq. (25) and $S(\mathrm{RH}(z))$ from Eq. (27). This completes the modeling of aerosol backscatter and extinction, using radiosonde RH as input.

3.3 Cloud backscatter and extinction

Cloud backscatter and extinction coefficients show large variability of several orders of magnitude, depending on cloud type and laser wavelength. Table 3 is extracted from Vaughan (2002) and has been used in various Aeolus studies.

Section 3.1 discussed the detection of cloud layers over De Bilt from radiosonde relative humidity and temperature. The next step is to discriminate between water and

AMTD
7, 1393–1455, 2014

ice clouds. Radiosonde temperature can also be used for this purpose; clouds with temperature at cloud base below 0 °C can be assumed an ice cloud, clouds with temperature at cloud top above 0 °C can be assumed water cloud. If the temperature at cloud base is above 0 °C and at cloud top below zero 0 °C then the cloud is composed of either ice, water, or a mixture. Liu et al. (2005) used MODIS data to quantify the observed frequency of cloud ice and water as a function of cloud temperature. They found that if the temperature at cloud top is below −17.16 °C, the probability of being a water cloud is less than 20 %. From the cloud extinction coefficients in Table 3 and from CALIPSO experience it is clear that the Aeolus laser beam will not be able to penetrate clouds with a substantial fraction of water droplets. On the other hand, clouds mainly composed of ice particles can be penetrated, depending on cloud thickness. Based on this we use the following criterion to classify clouds as either water or ice cloud: if the cloud top temperature is below −17.16 °C the cloud is classified as an ice cloud otherwise as a water cloud.

4 Analysis and discussion

The radiosonde-based cloud detection method, discussed in Sect. 3.1, has been applied to one year of radiosonde data measured at De Bilt in 2007. The results are validated against independent satellite data from Cloudsat/CALIPSO and ECMWF model data. The aerosol backscatter and extinction parameterization discussed in Sect. 3.2 is validated against UV lidar data measured from the Cabauw observation site, about 35 km from De Bilt.

4.1 Validation of radiosonde cloud detection

In this subsection, cloud layers detected from radiosonde data are compared against independent observations from CloudSat/CALIPSO and ECMWF data from the 2007 operational model version.

AMTD
7, 1393–1455, 2014

CloudSat is part of the A-train, orbiting at 705 km altitude and carries the nadir-looking millimeter-wavelength Cloud Profiling Radar (CPR) that is operated at 94 GHz to measure the power backscattered by clouds as a function of distance from the radar. The measurement footprint for a single profile is about 1.3 km across track by 1.7 km along track. Each profile is composed of 125 vertical bins. Each bin is approximately 240 m thick. A range resolution volume (RRV) is defined by the footprint and a 240 m range bin (Mace et al., 2007a).

CALIPSO is also part of the A-train and carries the two-wavelength Cloud-Aerosol Lidar with Orthogonal Polarization (CALIOP). CALIOP is a three-channel backscatter lidar to measure atmosphere backscattered signals optimized for aerosol and cloud profiling. The lidar emits laser pulses at 532 nm and 1064 nm and at a pulse repetition frequency of about 20 Hz. The fundamental vertical and horizontal sampling resolutions of the lidar are 30 m and 333 m respectively, to yield profiles from the earth surface up to 40 km. Additional information is found in Winker (2006).

With the ability of the CPR to probe optically thick large-particle layers and the ability of the CALIOP to sense optically thin cloud layers and aerosol, the two complementing instruments have the potential of providing a complete picture of the presence of cloud and aerosol along the A-train track. Two CloudSat standard data products, publicly available as the 2B-GEOPROF and 2B-GEOPROF-Lidar products (available at http://www.cloudsat.cira.colostate.edu/), have been used in the underlying study. The 2B-GEOPROF product identifies those levels in the vertical column sampled by CloudSat that contain significant radar echoes from hydrometeors, yielding the CPR cloud mask. CPR cloud mask values in the range of 20–40 implies that hydrometeors are detected in the radar RRV. An estimate of the radar reflectivity factor for each of these volumes is also provided with a CPR minimum detectable signal of −30 dBZ. The 2B-GEOPROF-Lidar product is the result of combined radar and lidar sensors. The most important information provided by the 2B-GEOPROF-Lidar product is the location of hydrometeor layers in the vertical column. The 2B-GEOPROF-Lidar product also includes an estimate of the fraction of lidar volumes in a CPR radar range resolution

AMTD
7, 1393–1455, 2014

volume that contains hydrometeors, that is denoted as cloud fraction. In this study, the radar reflectivity, CPR cloud mask and cloud fraction products are used to decide on cloud presence in a volume as follows: if radar reflectivity is above −30 dBZ and the CPR cloud mask value is above 20; or the cloud fraction is above 99 %, then cloud is assigned to the volume, otherwise there is no cloud.

4.1.1 Validation of cloud layer detection from radiosondes with CloudSat/CALIPSO

An example of cloud layers detected from radiosonde observations and the corresponding CloudSat/CALIPSO data are shown in Figs. 3 and 4, respectively. In Fig. 3, the light gray region and the light blue regions are the locations of cloud in the middle and right panel, respectively. The figure illustrates that four cloud layers are detected by WR95 and three cloud layers by Zhang (2010). Cloud base (top) heights detected by WR95 are 0.030 (0.493) km, 0.795 (2.124) km, 4.915 (7.956) km and 8.932 (10.908) km, respectively. Zhang2010's gives is 0.1 (2.1) km, 4.9 (7.9) km and 8.9 (12.1) km, respectively. The difference is mainly explained by the different processing methods on the separation distance between two consecutive layers for a multilayered cloud scene. In addition, different threshold values for RH of both methods give slightly different results on cloud base and top. Also note the big gap for the RH profiles for water and ice, showing the need for the recalculation discussed in Sect. 3.1.

The cloud layers were also detected by the algorithm of CloudSat/CALIPSO. Figure 4 shows that only two cloud layers (lower and middle) are detected by CPR, the upper cloud is detected by CALIOP. This example demonstrates the complementary of the CloudSat and CALIPSO products. Moreover, the two contiguous layers of middle and upper observed by CloudSat/CALIPSO are considered as a single-layer cloud, because the distance between the layers is less than 480 m. Therefore two cloud layers have been detected by CloudSat/CALIPSO with cloud base (top) heights of 1.1 (2.4) km and 3.6 (12.2) km respectively. There are several reasons for the difference between the cloud layers detected from radiosonde and CloudSat/CALIPSO. First, the mismatch in

AMTD
7, 1393–1455, 2014

time (about half an hour) and location of both measurements; the distance between De Bilt and the nearest satellite track location is 36 km. In addition the radiosonde drift from the launch location has not been taken into account. Second, the different vertical resolution of the two measurements: radiosonde (10 m) and CloudSat/CALIPSO (240 m). As a consequence the latter may fail to detect thin cloud layers. Third, signals of CloudSat/CALIPSO may strongly attenuate thus hampering to penetrate dense water clouds and fail to detect accurately the cloud base or underlying cloud layers. This is a potential problem in the tropics with deep convective clouds but less in the extra-tropics (De Bilt). Fourth, the threshold values (Table 2) set for cloud detection from radiosonde data may be good on average but non-optimal for specific scenes.

4.1.2 Comparison of radiosonde and satellite cloud parameters

The location, thickness and composition of cloud layers is important for many reasons, among others for atmospheric radiative and latent heating, for the validation of NWP models and the height assignment of atmospheric motion wind vectors (AMV) derived from time series of satellite cloud images. Here, we compare a number of cloud layer location parameters as retrieved from radiosondes with those from the CloudSat/CALIPSO products. These parameters include: the mean cloud base height of cloud layers (denoted mean cloud base), the mean cloud top height of cloud layers (denoted mean cloud top) and the mean cloud top height of the uppermost cloud layer (denoted upper cloud top). Observation matching in time and space has been taken into account in the intercomparison as follows: the time difference between the observations is less than one hour and the distance less than 40 km. For the 1 yr 2007 period only 20 samples fulfilled these requirements.

Figure 5 shows scatterplots of the cloud parameters between radiosonde measured by WR95 and Zhang2010 and CloudSat/CALIPSO. The correlation coefficients for mean-cloud base, mean-cloud top and upper-cloud top are 0.809, 0.833 and 0.941 respectively for WR95 vs. Cloudsat/CALIPSO, and 0.895, 0.898 and 0.955 for Zhang2010 vs. Cloudsat/CALIPSO. Taking CloudSat/CALIPSO as reference, there is

AMTD
7, 1393–1455, 2014

a better agreement of cloud parameters from Zhang2010 than from WR95. The correlation values are high considering the fundamental differences of both datasets as discussed in the previous section. However, the number of samples is too small to draw firm conclusions.

4.1.3 Comparison of radiosonde and ECMWF cloud cover

Cloud cover refers to the fraction of the sky covered by clouds at a weather model level in a particular grid box. Cloud cover is a standard output product of the ECMWF model and available from their MARS (meteorological archiving system) archive. Non-zero cloud cover at a certain model level means that part of the model grid box is filled with cloud, i.e., a value of 0.3 means that 30 % of the model grid box is filled with cloud. In this section cloud cover retrieved from radiosondes with the WR95 and Zhang2010 methods is validated against cloud cover from the ECMWF model. Mean cloud cover, $\overline{\mathrm{cc}}$, at radiosonde altitude z_R from WR95 and Zhang2010 is obtained as follows:

(1) If there is a cloud layer detected at radiosonde level j with altitude $z_\mathrm{R}(i)$ for radiosonde launch numbered j then $\mathrm{cc}_\mathrm{R}(z_\mathrm{R}(i),j,k)=1$, otherwise $\mathrm{cc}_\mathrm{R}(z_\mathrm{R}(i),j,k)=0$ (with $k=\{1,2\}$ standing for WR95 and Zhang2010, respectively).

(2) Averaging the cloud cover for all N radiosonde retrievals over the 1 yr 2007 period yields the mean cloud cover for each altitude z_R:

$$\overline{\mathrm{cc}_\mathrm{R}}(z_\mathrm{R}(i),k)=\frac{1}{N}\sum_{j=1}^{N}\mathrm{cc}_\mathrm{R}(z_\mathrm{R}(i),j,k) \tag{29}$$

Similarly, for the ECMWF model mean cloud cover is obtained but at model level l with altitude, $z_\mathrm{M}(l)$: $\overline{\mathrm{cc}}_\mathrm{M}(z_\mathrm{M}(l))$. For a fair intercomparison of radiosonde and ECMWF model cloud cover, the calculated mean radiosonde cloud cover is averaged over M_l radiosonde levels around the model level l:

AMTD
7, 1393–1455, 2014

$$\overline{\mathrm{cc_R}}(z_\mathrm{M}(l),k) = \frac{1}{M_l}\sum_{i=1}^{M_l}\overline{\mathrm{cc_R}}(z_\mathrm{R}(i),k) = \frac{1}{NM_l}\sum_{i=1}^{M_l}\sum_{j=1}^{N}\mathrm{cc_R}(z_\mathrm{R}(i),j,k) \quad (30)$$

This is done for all model levels l. Figure 6 shows that both the WR95, from $\overline{\mathrm{cc_R}}(z_\mathrm{M}(l),1)$, and Zhang2010, from $\overline{\mathrm{cc_R}}(z_\mathrm{M}(l),2)$, method overestimate cloud coverage below 8 km and underestimate cloud coverage above 8 km relative to ECMWF, from $\overline{\mathrm{cc_M}}(z_\mathrm{M}(l))$. This result agrees well with Houchi (2013) who showed an underestimate of ECMWF model cloud below 8 km and an overestimate above 8 km relative to the CALIPSO level-2 product. Overall, the Zhang2010 result is closer to ECMWF than WR95. The correlation coefficient between ECMWF and Zhang2010/WR95 is 0.9064/0.7275. Also, the Zhang2010 method fits better to the CALIPSO level-2 product presented in Houchi (2013).

Based on these results and the results in the previous sections we use the cloud layer detections from the Zhang2010 method in the remainder of this paper. For cloud backscatter and extinction we use Table 3 and the temperature from the radiosonde as discussed in Sect. 3.3.

4.2 Aerosol backscatter and extinction

The previous section discussed atmospheric backscatter and extinction from clouds derived from radiosonde data. Besides clouds, aerosols and molecules determine the scattering properties of the atmosphere. Molecular backscatter and extinction is relatively easily obtained from atmospheric pressure and temperature (Marseille and Stoffelen, 2003). Aerosol density and composition are much more variable in space and time than molecules and the scattering and extinction properties depend on aerosol type and relative humidity.

The CALIPSO lidar provides aerosol backscatter and aerosol type but at relatively low resolution for moderate aerosol density. In addition, the number of samples with

AMTD
7, 1393–1455, 2014

combined wind and temperature from radiosondes is small as discussed in the previous section. Alternatively, Raman lidars are operated to measure aerosol backscatter and extinction simultaneously (e.g. Liu et al., 2002 and Rogers et al., 2006). Unfortunately a Raman lidar was not operated during the 2007 study period in De Bilt nor at the nearby measurement site in Cabauw. However, a UV lidar operated at the Aeolus wavelength of 355 nm has been in regular operation in Cabauw since July 2007. A major disadvantage of a ground-based lidar is blocking of the signal by low-level clouds obscuring the atmosphere aloft. No aerosol information can be retrieved above clouds.

Instead we propose the parameterization discussed in Sect. 3.2 that is validated in this section against the UV lidar data from Cabauw for cloud-free scenes.

The simulation of hygroscopic growth factor, $f_{\mathrm{scatt}}(\mathrm{RH})$, for tropospheric marine aerosol as a function of RH is calculated using Eq. (24), see Fig. 7. The figure shows a modest increase of the growth factor from 1 to 2 with increasing RH up to 80 % then increasing fast to a maximum value of 6 for RH values above 80 %. This is explained by the swelling tendency of the aerosol particles for RH values exceeding the deliquescent point. This trend is compatible with partially soluble aerosol particles characterized by a deliquescent growth. The deliquescent point is at about 78 % RH, that is close to those reported for pure sodium chloride (75.3 %, Tang and Munkelwitz, 1993) and pure ammonium sulphate (79.6 %, Onasch et al., 1999) measured at 25 °C.

Simultaneously, the lidar ratio S as a function of RH at 355 nm for De Bilt station is simulated using Eq. (27), see also Fig. 7. The simulation result illustrates that S grows from 42.5 to 70 (sr) for RH increasing from 0 % to 100 %. At 355 nm wavelength, the uncertainty range is between ±1 % and ±14 % (Ackermann, 1998).

4.2.1 A case study

An example of total atmospheric backscatter and extinction retrieved from radiosonde data along its track is given below. Figure 8 shows relative humidity and temperature as a function of altitude from as observed by the radiosonde. The radiosonde reached

AMTD
7, 1393–1455, 2014

an altitude of about 25 km. Three cloud layers are detected by the Zhang2010 method, the heights of cloud base are 5.4 km, 7.7 km and 9.9 km, respectively.

The top row of Fig. 9 shows the corresponding growth factor from Eq. (24) and lidar ratio from Eq. (27) assuming dominant maritime aerosol presence over the Netherlands. Aerosol backscatter and extinction are obtained from Eqs. (25) and (28). Total particle backscatter and extinction from aerosol and cloud is shown in the bottom row of Fig. 9. From the figure it is clear that the backscatter profile deviates substantially from the climatological profile for RH exceeding 80 % and for cloud layers. Because the temperatures at the cloud bases are below −20 °C, the clouds are all considered ice clouds and backscatter and extinction are obtained from Table 3, assuming cirrus cloud type, i.e., cloud backscatter and extinction coefficients are 1.4×10^{-5} ($m^{-1}\,sr^{-1}$) and 2.0×10^{-4} (m^{-1}), respectively. It is clear that cloud backscatter and extinction are an order of magnitude larger than aerosol backscatter and extinction.

4.2.2 Validation with ground-based lidar data

Aerosol density exhibits large variability in both time and space. Total aerosol density within the sampling volume determines the signal strength of the backscattered signal on the Mie receiver that is related directly to the random error of the retrieved Mie channel wind (Marseille, 2003). Besides total aerosol density, the variability of aerosol density within Aeolus bins is important for the quality of Aeolus winds that may cause biases of retrieved winds in case of substantial wind-shear over the bin as discussed in Sect. 2. The simulated total aerosol backscatter and backscatter variability from the radiosonde observations, discussed in the previous section, are compared with real ground-based lidar observations from the UV lidar at the Cabauw observation site (51.97° N, 4.926° E) located about 30 km from De Bilt. The UV lidar is a compact vertically pointing (non-scanning) lidar with orthogonal polarization and using a frequency tripled Nd:YAG laser transmitting 12 mJ pulses of 355 nm wavelength at 20 Hz. The detection range is about 20 km. The UV lidar is operational since 5 July 2007.

AMTD
7, 1393–1455, 2014

The UV lidar product includes backscatter profiles (both perpendicular and parallel) for 30 s accumulation intervals with a vertical resolution of 15 m. To improve the signal-to-noise of the UV lidar data, lidar profiles were averaged over 30 min intervals centered at 12:00 UTC before comparing with 12:00 UTC radiosonde profiles. For the intercomparison only cloud-free scenes were considered over the period 5 July 2007 until the end of 2007. A total of 48 cloud-free scenes were found. The aerosol backscatter estimates were derived from the lidar attenuated backscatter signals using a Klett–Fernald approach (Klett, 1985; Fernald, 1984) with an assumed S ratio of 50 sr which is appropriate for urban aerosols (Müller et al., 2007). Using a S value appropriate for maritime aerosols (20 sr) (Groß et al., 2011) leads to a retrieved backscatter values which are about 40–80 % higher at 0.5 km and 20–40 % higher at 1.0 km with diminishing differences above this height.

Figure 10 shows that both the average aerosol backscatter from radiosondes and the UV lidar show a constant backscatter from the surface up to 500 m (800 m for the UV lidar) then dropping by an order of magnitude (slightly less for the UV lidar) for altitudes up to 2 km. Near the surface the median aerosol backscatter from the UV lidar is a factor of about 4 smaller than from the radiosonde. Here we note that the magnitude of the radiosonde aerosol backscatter is strongly related to the climatological RMA profile that was obtained from flight campaigns over the Northern and Southern Atlantic in 1989 as discussed in Sect. 3.2 and thus not expected representative for De Bilt in 2007. The comparison with the UV lidar values is also be impacted by the fact that the lidar overlap function is incomplete below 300 m so that the lidar values below this altitude are simple extrapolations from higher altitude values. The larger spread of the quartile profiles for the UV lidar indicates that the distribution of aerosol backscatter from radiosondes is underdispersive. To further elaborate on this we consider a typical bin size for the Aeolus Mie channel in the boundary layer of 250 m. The difference between the maximum and minimum backscatter value within the bin is a measure of backscatter variability, $\delta\beta$, and calculated, for 250 m bins, from:

$$\delta\beta_i = [\max(\beta_i) - \min(\beta_i)]/250 \quad (31)$$

AMTD
7, 1393–1455, 2014

for range gate intervals $[250 \cdot (i-1), 250 \cdot i]$ m, $i = 1, \ldots, 8$, $\max(\beta_i)$ and $\min(\beta_i)$ are the maximum and minimum backscatter value in bin i respectively.

Also the aerosol backscatter variability shows an increase from the surface in the lower part of the boundary layer for both the radiosonde and UV lidar in Fig. 11 and then decreasing for altitudes up to 2 km. The radiosonde median profile is generally larger than from the UV lidar suggesting larger variability within 250 m bins from the radiosonde aerosol backscatter. However, the substantially smaller/larger lower/higher decile curves for the UV lidar suggest that scenes observed by the lidar are more heterogeneous than those simulated for the radiosonde. Random instrument noise is a small factor here given the 30 min averaging of lidar attenuated backscatter before processing.

In conclusion, the aerosol backscatter variability simulated from radiosonde observations is representative for real atmospheric scenes as measured by the UV lidar with an overestimate (on average) in the lowest 700 m of the boundary layer.

5 Application to the Aeolus mission

It was mentioned in Sect. 1 that non-homogeneous atmospheric conditions within Aeolus observation bins cause errors in retrieved winds. In Sect. 2 an analytical expression was derived to quantify the wind error. In this section we use the high vertical resolution (10 m) database of collocated winds and atmosphere optical characterization at 355 nm (i.e., the Aeolus laser wavelength) both obtained from De Bilt radiosondes, i.e., winds obtained directly from the instrument data and the optical properties simulated as discussed in Sects. 3 and 4. In the remainder this is referred to as the radiosonde database. To estimate Aeolus biases for real atmospheric scenes, Eqs. (1) and (2) are applied to the radiosonde database. The database includes wind, temperature, pressure, relative humidity, aerosol and cloud backscatter and extinction at 10 m resolution. Signal extinction through molecular scattering is wavelength dependent and may be theoretically determined from the Rayleigh scattering law

AMTD
7, 1393–1455, 2014

and knowledge of the atmospheric temperature and pressure (Marseille and Stoffelen, 2003). Molecular backscatter, $\beta_m(\lambda, z)$ ($m^{-1} sr^{-1}$), is related to molecular extinction, $\alpha_m(\lambda, z)$ (m^{-1}), through a backscatter-to-extinction coefficient $b_m(\lambda) = 3/8\pi$ (sr^{-1}): $\beta_m(\lambda, z) = \alpha_m(\lambda, z) b_m(\lambda)$. The radiosonde database thus contains all ingredients to calculate Eqs. (1) and (2) and the Aeolus wind error profile $u_k^M - u^T$, $k = \{p, m\}$, as a function of Aeolus bin size. The error profiles are calculated for each day of the year 2007 from which the wind error bias and standard deviation are calculated for each height bin.

It is noted that the Aeolus level-2 processor (L2Bp) includes a classification algorithm that decides on the presence of particles inside the measurement bin. The decision is based on an estimate of the scattering ratio from the Mie channel signal (Tan et al., 2008a, b) that is defined as the ratio of total backscatter (from aerosol plus cloud plus molecules) and molecular backscatter. The value is always larger than 1 and a threshold value of 1.2 has been selected as default value in the latest version of the L2Bp. Bins with a scattering ratio exceeding the threshold value are assigned as particle bins, otherwise as particle-free bins. For consistency with the L2Bp the same procedure is applied to the processing of the radiosonde database: mie winds are obtained only for bins with the scattering ratio exceeding the threshold value.

The Mie wind error statistics in the left panel of Fig. 12 show that both the wind error bias and standard deviation increase for increasing bin size, as expected since atmospheric variability increases with length scale. Near the surface 250 m Mie bins are foreseen for zero-wind calibration from surface returns. At higher altitudes, larger Mie bins are foreseen because of decreasing aerosol content with altitude, on average, and to enable Mie wind retrieval at altitudes in the upper troposphere, with only a total number of 24 available vertical bins. For 1000 m Mie bins, the Mie wind error standard deviation through atmospheric heterogeneity is between 1 and 1.5 ms^{-1} for most part of the free troposphere and lower stratosphere, i.e., of similar magnitude as the Mie channel instrument noise error standard deviation of about 1 ms^{-1} (Marseille et al., 2013). For 2000 m bin size the error standard deviation is about doubled. For 500 m

AMTD
7, 1393–1455, 2014

bins the error standard deviation is between 0.5 and 1 ms^{-1}. However, note that for 500 m bins the maximum altitude for Mie wind observations is chosen always below 12 km, due to the limitation to 24 vertical bins.

Figure 13 zooms in on the lower part of the atmosphere and compares three different particle regimes. Wind is obtained from the radiosonde database. For a smooth distribution of particles, following the climatological RMA profile introduced in Sect. 3.2, the Mie wind error is small: below 0.1/0.2 ms^{-1} for 250/500 m bins. For the more realistic aerosol variability from the parameterization of Eq. (25), the Mie wind errors are 0.1–0.2/0.2–0.4 ms^{-1} for 250/500 m bins. Because of increased aerosol density relative to the RMA, Mie winds are obtained up to 2.5 km as compared to 1.5 km for the RMA regime. Above these altitudes the aerosol density is too low for Mie wind retrieval. Finally, considering the complete particle distribution including clouds further substantially increases the error of Mie winds. Note that additional errors due to horizontal variability (e.g., aerosol and cloud variability due to PBL eddies) are still ignored here.

It is concluded that Aeolus Mie wind quality is sensitive to the vertical heterogeneity of the atmosphere, in particular for scenes with cloud layers; Mie winds from cloud layers show large errors at all altitudes. The same is most probably true for thick aerosol layers (for instance desert dust) and horizontal structures, although not explicitly studied here. These conclusions are well in line with the theoretical analysis of Sect. 2. In moderate aerosol regimes the corresponding Mie wind errors are much smaller than the instrument noise. Based on these conclusions it is recommended to separate Mie winds obtained from optically thin (moderate aerosol) and optically thick (cloud and dense aerosol) atmospheric layers. Discrimination between both regimes may be done from the available scattering ratio and/or the layer optical thickness. Calculation of the latter is not yet part of the L2Bp.

The data coverage in the right panel of Fig. 12 shows a strong peak around 1.5 km which corresponds to the average top of the boundary layer over De Bilt at 12:00 UTC. Below the boundary top Mie winds are obtained from both aerosol and cloud scattering. At higher altitudes, Mie winds are from cloud scattering only. The probability of

AMTD
7, 1393–1455, 2014

encountering cloud increases for larger bin sizes, explaining the increasing number of observations with increasing bin size as a function of bin altitude in the right panel of Fig. 12. However, the total number of Mie winds decreases with increasing bin size, which is explained by noting that for instance a single 2000 m bin includes eight 250 m bins.

In Sect. 4.2 it was found that the aerosol backscatter variability in the radiosonde database well represents the real atmosphere as observed by the UV lidar from which we conclude that the above statements well translate to real atmospheric scenes.

Figure 14 show the statistics for Rayleigh winds. Above 13 km, no clouds were detected by the Zhang2010 method for the 2007 radiosondes over De Bilt and aerosol density and density variations are negligible. However, temperature and pressure vary and thus molecular backscatter and extinction also vary inside the Rayleigh bins. This explains the non-zero error above 13 km, but with an error standard deviation of only a few tenths of a ms^{-1}. Below 13 km, the Rayleigh wind error increases substantially (solid lines). Above the boundary layer this is due to cloud layers that cause a non-homogeneous backscattering from the measurement bin from molecules, due to cloud extinction. Inside the boundary layer the wind error further increases because of the additional extinction from aerosol. The Rayleigh channel wind errors are substantially smaller than from the Mie channel, in line with the theoretical analysis of Sect. 2. As for Mie winds, the errors increase with increasing bin size. For typical Rayleigh bin sizes of 1000 m in the free troposphere the error standard deviation is generally well below 0.5 ms^{-1}. This result is further improved through the classification procedure discussed above. The dashed lines in the left panel of Fig. 14 show the Rayleigh wind error standard deviation when using only Rayleigh winds for bins with a scattering ratio below 1.2, i.e., ignoring cloud contaminated bins. Errors from Rayleigh channel winds then become negligible. This is however at the expense of data coverage as observed from the right panel of Fig. 14: fewer winds are obtained between 2 and 13 km and no Rayleigh winds are obtained below 2 km when applying classification. In the absence of clouds and aerosol above 13 km data coverage is identical for all bin sizes

AMTD
7, 1393–1455, 2014

and classification is not needed. Note also convergence of the dashed and solid lines near 13 km altitude and overlap above 13 km in the left panel of Fig. 14.

Rayleigh channel data coverage is also reduced below 8 km in the absence of classification (solid lines in the right panel). This is because clouds obscure the lower part of the atmosphere. A 2-way transmission threshold value of 0.1 was used here, i.e., if the laser signal transmission drops below the threshold value then no valid Rayleigh winds can be retrieved because of too low SNR.

Finally, it should be said that Rayleigh winds meeting the mission requirement can only be obtained for bin sizes larger than 1000 m (Marseille et al., 2013). The red and dark blue curves of Fig. 14 are thus artificial and no valid options for the Rayleigh channel of the Aeolus mission. Note, however, that smaller vertical bins are useful for a more effective quality control of optically variable scenes.

6 Summary and conclusions

Observation biases are known to be detrimental when gone undetected in NWP. The ESA Aeolus mission aims to measure wind profiles from space from the received backscattered signal from atmospheric particles (aerosol and cloud droplets) and molecules. Retrieved winds may suffer from biases induced by instrument imperfections and atmosphere heterogeneous conditions, i.e., varying backscatter and wind inside Aeolus measurement volumes (bins). In preparation for launch this study aimed to quantify the expected bias in Mie and Rayleigh channel winds caused by atmospheric heterogeneity. In addition recommendations were formulated to improve level-2 processing to identify such scenes and apply quality control before using the observations in NWP.

A realistic assessment of Aeolus wind errors from atmospheric heterogeneity requires a database of combined wind and atmosphere optical properties at substantial higher resolution than the Aeolus observation sampling volume, that is 86 km along satellite track and several hundreds of meters to 2 km in the vertical, where it is noted

AMTD
7, 1393–1455, 2014

that the volume is oversampled along track by 30 measurements of about 2.88 km length. Available databases either lack resolution or one of the database ingredients.

High-resolution radiosondes provide profiles of wind vectors at 10 m (vertical) resolution. Here we presented a method to simulate co-located cloud and aerosol optical properties from radiosonde observations to complete the high resolution database. Two methods to detect clouds along the radiosonde path from measured relative humidity (RH) and temperature were compared from which the Zhang (2010) method performed best. Detected clouds are classified based on cloud altitude and temperature. Standard values from literature are used for cloud backscatter and extinction for each cloud type. Aerosol backscatter is simulated from a climatological profile adapted by a RH-dependent growth factor which addresses the hygroscopic effect of aerosol scattering. Aerosol extinction is simulated by multiplying aerosol backscatter with a RH-dependent lidar ratio.

Detected cloud layers with the Zhang (2010) method were compared against the CloudSat/CALIPSO level-2 cloud mask product for the 2007 one-year period showing good agreement. Comparison against ECMWF model winds also showed good agreement and confirmed the bias of ECMWF 2007 model clouds with an underestimate of model clouds below 8 km and an overestimate of model clouds above 8 km, in agreement with Houchi (2013).

Simulated aerosol backscatter was compared against real atmospheric measurements from the operational UV lidar in Cabauw and showed larger values by a factor of 4 below 700 m altitude and thus potentially overestimating Aeolus Mie wind coverage in the lower part of the boundary layer. Also, the distribution of simulated backscatter is underdispersive. However, the mean aerosol backscatter variability within 250 m Aeolus bins in the lower 2 km of the atmosphere agrees well between both datasets, implying that wind error biases calculated from the radiosonde database are expected to agree well with those from the real atmosphere.

The simulated aerosol backscatter and extinction along the radiosonde paths was based on the assumption of urban aerosol as the dominant source which is a good

AMTD
7, 1393–1455, 2014

approximation on average given the predominant westerly flow over the Netherlands and concentration of human activities in the coastal region west of De Bilt. Also, easterly winds from Germany transport industrial aerosol from the Ruhr area towards the Netherlands. A further fine tuning may be envisaged by an improved selection of aerosol type in the aerosol and extinction backscatter parameterizations by considering the large scale flow obtained from the radiosonde wind data, for instance northerly winds transporting clean marine aerosol from the North Sea.

The derived database from radiosonde launches over De Bilt is unique in the sense that it contains winds and atmospheric optics at very high (10 m) vertical resolution. The database has proven useful for evaluating Aeolus wind biases caused by atmospheric heterogeneity in the vertical. Since radiosondes probe the atmosphere along their path only additional errors due to horizontal variability (e.g., aerosol and cloud variability due to PBL eddies) have been ignored. However, Aeolus' oversampling of the 86 km along track integration length by 30 measurements enables detection of scenes with large horizontal variability and to apply quality control. Most uncertainty is on vertical heterogeneity, explaining the focus of this paper.

Analytical equations were derived to estimate the bias of Mie channel and Rayleigh channel winds in case of a particle layer inside the Aeolus bin whose location and thickness are unknown. The mean error for Mie channel winds equal zero but can be vary substantially from case to case. This was expressed by the error variance that grows quadratically with bin size and wind-shear over the observation bin. The error variance of a typical Mie channel observation in the troposphere with 1000 m bin size and a typical wind-shear of 4 ms^{-1} per km equals 1.33 $m^2 s^{-2}$, i.e., of the same order of magnitude as the random error. However, such systematic errors may extend over many observations, depending on the size of the cloud/aerosol layer, and are known to be detrimental for NWP of not properly treated. The mean error for Rayleigh channel winds is non-zero but grows linearly with bin size and wind-shear over the observation bin, but layer transmission is the dominant parameter. Typical values for the Rayleigh wind bias range from 0.1 ms^{-1} for optically thin cirrus clouds to 1 ms^{-1} for

AMTD
7, 1393–1455, 2014

dense (stratus) clouds for the same bin size and wind-shear as used above. The error variance for Rayleigh winds also grows quadratically with bin size and wind-shear over the observation bin, but is substantially smaller than for Mie winds with values ranging from 0.004 to 0.33 $m^2 s^{-2}$ for optically thin and dense clouds respectively and the same bin size and wind-shear as used above. Given the Aeolus mission requirement for zero-wind bias of HLOS winds of 0.4 ms^{-1}, it is concluded that although cloud and aerosol layers return strong signals to yield winds with small random error, the bias may be substantial, in particular for Mie channel winds, exceeding the mission requirement. One way to alleviate this problem is by reducing the Mie bin size.

The analytical equations were largely confirmed by calculations from the radiosonde database:

- the wind error standard deviation grows linearly with increasing bin size.
- Typical values for the Mie channel wind error standard deviation in the free troposphere are in the range 1–1.5 ms^{-1} for 1000 m bins, as compared to $\sqrt{1.33} = 1.15\,ms^{-1}$ from the analytical expression.
- Rayleigh channel wind errors through atmospheric heterogeneity are substantially smaller than Mie channel wind errors with values for the error standard deviation ranging from 0.1–1.2 ms^{-1} for 1000 m bins. This range is slightly broader than found from the analytical expression: $\sqrt{0.004} - \sqrt{0.33}$ or 0.06–0.57 ms^{-1}.

It is noted that Rayleigh wind error biases can be largely reduced by the classification procedure that is implemented in the Aeolus level-2 processor which selects measurements classified as particle-free before integrating to observation level. The reduced bias is at the expense of an increased random error and reduced data coverage, but the latter two are much less detrimental for NWP than systematic errors.

From the above it is clear that the level-2 classification procedure is of vital importance to reduce wind error biases (Rayleigh channel) and to detect winds with potential large biases that cannot be corrected for (Mie channel) but need special treatment before use in data assimilation, e.g., reducing their weight in the analysis or reject. For

AMTD
7, 1393–1455, 2014

Rayleigh channel bins, classification can be applied only in case of a corresponding Mie bin at the same altitude, which may not always be available, depending on the Mie and Rayleigh channel sampling strategy (Marseille et al., 2010). More advanced classification procedures are foreseen that rely on the Rayleigh channel signal only for instance to detect tropical cirrus and polar stratospheric clouds in case of missing Mie bins or Mie channel failure.

The presented method may be applied to other radiosondes in other climate zones to assess Aeolus wind errors for typical atmospheric conditions such as in the (sub-) tropics. In addition the results may be used to validate cloud products, in particular cloud layer height, retrieved from the European MeteoSat Second Generation geostationary satellite. Finally, atmospheric motion wind vectors (AMV), obtained from cloud feature tracking, are known to suffer from height assignment errors which reduce their impact in NWP. The cloud information from the radiosonde database can be used for the validation of AMVs or to correct for height assignment errors.

Acknowledgements. This study is supported by the National Natural Science Foundation of China (Grant No. 41205125). We would like to thank the Royal Netherlands Meteorological Institute (KNMI) for providing the Radiosonde RS92, the UV lidar and ECMWF model data sets. The CloudSat/CALIPSO data are provided by the NASA CloudSat project from their web site at http://www.cloudsat.cira.colostate.edu.

References

Ackermann, J.: The extinction-to-backscatter ratio of tropospheric aerosol: a numerical study, J. Atmos. Ocean. Tech., 15, 1043–1050, 1998.

Alduchov, O. A. and Eskridge, E. E.: Improved Magnus form approximation of saturation vapor pressure, J. Appl. Meteorol., 35, 601–609, 1996.

Benayahu, Y., Ben-David, A., Fastig, S., and Cohen, A.: Cloud-droplet-size distribution from lidar multiple-scattering measurements, Appl. Optics, 34, 1569–1578, 1995.

AMTD

7, 1393–1455, 2014

Boucher, O. and Anderson, L.: General circulation model assessment of the sensitivity of direct climate forcing by anthropogenic sulfate aerosols to aerosol size and chemistry, J. Geophys. Res., 100, 26117–26134, 1995.
Carrier, L. W., Cato, G. A., and von Essen, K. J.: The backscattering and extinction of visible and infrared radiation by selected major cloud models, Appl. Optics, 6, 1209–1216, 1967.
Charlson, R. J., Langner, J., Rodhe, H., Leovy, C. B., and Warren, S. G.: Perturbation of the Northern Hemisphere radiative balance by backscattering from anthropogenic sulfate aerosols, Tellus AB, 43, 152–163, 1991.
Chen, W. N., Chiang, Ch. W., Nee, J. B.: Lidar ratio and depolarization ratio for cirrus clouds, Appl. Optics, 41, 6470–6476, 2002.
Chernykh, I. V. and Eskridge, R. E.: Determination of clouds amount and level from radiosonde soundings, J. Appl. Meteorol., 35, 1362–1369, 1996.
Chylek, P. and Damiano, P.: Polynomial approximation of the optical properties of water clouds in the 8–12 µm spectral region, J. Appl. Meteorol., 31, 1210–1218, 1992.
Covert, D. S., Waggoner, A. P., Weiss, R. E., Ahlquist, N. C., and Charlson, R. J.: Atmospheric aerosols, humidity and visibility, in: Character and Origin of Smog Aerosols, John Wiley, New York, 1979.
Curry, J. A., Rossow, W. B., Randall, D., and Schramm, J. L.: Overview of Arctic cloud and radiation characteristics, J. Climate, 9, 1731–1764, 1996.
Dermendjian, D.: Scattering and polarization properties of water clouds and hazes in the visible and infrared, Appl. Optics, 3, 187–196, 1964.
ESA: ADM-Aeolus science report, avialable at: http://esamultimedia.esa.int/docs/SP-1311_ADM-Aeolus_FINAL_low-res.pdf (last access: 10 February 2014), 2008.
Evans, B. T. N.: Sensitivity of the backscatter/extinction ratio to changes in aerosol properties: implications for lidar, Appl. Optics, 27, 3299–3305, 1988.
Evans, B. T. N. and Fournier, G. R.: Simple approximations to extinction efficiency valid over all size parameters, Appl. Optics, 29, 4666–4670, 1990.
Fernald, F. G.: Analysis of atmospheric lidar observations: some comments, Appl. Optics, 23, 652–653, 1984.
Gasso, S., Hegg, D. A., Covert, D. S., Collins, D., Noone, K. J., Oström, E., Schmid, B., Russel, P. B., Livingston, J. M., Durkee, P. A., and Josson, H.: Influence of humidity on the aerosol scattering coefficient and its effect on the upwelling radiance during ACE-2, Tellus B, 52, 546–567, 2000.

AMTD
7, 1393–1455, 2014

Gayet, J.-F., Stachlewska, I. S., Jourdan, O., Shcherbakov, V., Schwarzenboeck, A., and Neuber, R.: Microphysical and optical properties of precipitating drizzle and ice particles obtained from alternated lidar and in situ measurements, Ann. Geophys., 25, 1487–1497, doi:10.5194/angeo-25-1487-2007, 2007.

Groß, S., Tesche, M., Freudenthaler, V., Toledano, C., Wiegner, M., Ansmann, A., Althausen, D., and Seefeldner, M.: Characterization of Saharan dust, marine aerosols and mixtures of biomass-burning aerosols and dust by means of multi-wavelength depolarization and Raman lidar measurements during SAMUM 2, Tellus B, 63, 706–724, 2011.

Hänel, G.: The properties of atmospheric aerosol particles as functions of the relative humidity at thermodynamic equilibrium with the surrounding moist air, Adv. Geophys., 19, 73–188, 1976.

Hegg, D., Larson, T., and Yllen, P.-F.: A theoretical study of the effect of relative humidity on light scattering by tropospherical aerosols, J. Geophys. Res., 98, 18435–18439, 1993.

Houchi, K.: On High Resolution Wind, Shear and Cloud Vertical Structures – Preparation of the Aeolus Space Mission, PhD Thesis, 2013.

Houchi, K., Stoffelen, A., Marseille, G. J., and Kloe, J. D.: Comparison of wind and wind shear climatologies derived from high-resolution radiosondes and the ECMWF model, J. Geophys. Res., 115, D22123, doi:10.1029/2009JD013196, 2010.

Immler, F., Krüger, K., Tegtmeier, S., Fujiwara, M., Fortuin, P., Verver, G., and Schrems, O.: Cirrus clouds, humidity, and dehydration in the tropical tropopause layer observed at Paramaribo, Suriname (5.8° N, 55.2° W), J. Geophys. Res., 112, D03209, doi:10.1029/2006JD007440, 2007.

Intergovernmental Panel on Climate Change (IPCC): IPCC Special Report on Renewable Energy Sources and Climate Change Mitigation, edited by: Edenhofer, O., Madruga, R. P., Sokona, Y., Seyboth, K., Matschoss, P., Kadner, S., Zwickel, T., Eickemeier, P., Hansen, G., Schlömer, S., and Stechow, C. V., Cambridge University Press, London, 2012.

Kasten, F.: Visibility forecast in the phase of pre-condensation, Tellus, 21, 631–635, 1969.

Klett, J. F.: Lidar inversion with variable backscatter/extinction ratios, Appl. Optics, 24, 1638–1643, 1985.

Kotchenruther, R. A., Hobbs, P. V., and Hegg, D. A.: Humidification factors for atmospheric aerosol off the mid-Atlantic coast of United States, J. Geophys. Res., 104, 2239–2252, 1999.

Lin, Z. J., Tao, J., Chai, F. H., Fan, S. J., Yue, J. H., Zhu, L. H., Ho, K. F., and Zhang, R. J.: Impact of relative humidity and particles number size distribution on aerosol light extinction

AMTD
7, 1393–1455, 2014

in the urban area of Guangzhou, Atmos. Chem. Phys., 13, 1115–1128, doi:10.5194/acp-13-1115-2013, 2013.
Liu, Z., Sugimoto, N., and Murayama, T.: Extinction-to-backscatter ratio of Asian dust observed with high-spectral-resolution lidar and Raman lidar, Appl. Optics, 41, 2760–2766, 2002.
Liu, Z. Y., Omar, A. H., Hu, Y. X., Vaughan, M. A., and Winker, D. M.: CALIOP algorithm theoretical basis document, part 3: Scene classification algorithms, avialable at: http://www-calipso.larc.nasa.gov/resources/pdfs/PC-SCI-202_Part3_v1.0.pdf (last access: 10 February 2014), 2005.
Mace, G. G., Marchand, R., Zhang, Q., and Stephens, G. L.: Global hydrometeor occurrence as observed by CloudSat: Initial observations from summer 2006, Geophys. Res. Lett., 34, L09808, doi:10.1029/2006GL029017, 2007a.
Malm, W. C., Day, D. E., Kreidenweis, S. M., Collett, J. L., and Lee, T.: Humidity-dependent optical properties of fine particles during the Big Bend Regional Aerosol and Visibility Observational Study, J. Geophys. Res., 108, 4279, doi:10.1029/2002JD002998, 2003.
Marseille, G. J. and Stoffelen, A.: Simulation of wind profiles from a space-borne Doppler wind lidar, Q. J. Roy. Meteorol. Soc., 129, 3079–3098, 2003.
Marseille, G. J., Stoffelen, A., and Barkmeijer, J.: Sensitivity Observing System Experiment (SOSE) – a new effective NWP-based tool in designing the global observing system, Tellus A, 60, 216–233, 2008.
Marseille, G. J., Stoffelen, A., Schyberg, H., Körnich, H., and Megner, L.: VAMP – Vertical Aeolus Measurement Positioning, ESA Study Final Report, Contract 20940/07/NL/JA, 2010.
Marseille, G. J., Houchi, K., de Kloe, J., and Stoffelen, A.: The definition of an atmospheric database for Aeolus, Atmos. Meas. Tech., 4, 67–88, doi:10.5194/amt-4-67-2011, 2011.
Marseille, G. J., Stoffelen, A., Schyberg, H., Körnich, H., and Megner, L.: VHAMP – Vertical and Horizontal Aeolus Measurement Positioning, ESA Study Final Report, CCN2 to Contract 20940/07/NL/JA, 2013.
Müller, D., Ansmann, A., Mattis, I., Tesche, M., Wandinger, U., Althausen, D., and Pisani, G.: Aerosol-type-dependent lidar ratios observed with Raman lidar, J. Geophys. Res., 112, D16202, doi:10.1029/2006JD008292, 2007.
Norris, J. R.: Multidecadal changes in near-global cloud cover and estimated cloud cover radiative forcing, J. Geophys. Res., 110, D24113, doi:10.1029/2004JD005600, 2005.
Onasch, T. B., Siefert, T. L., Brooks, S. D., Prenni, A. J., Murray, B., Wilson, M. A., and Tolbert, M. A.: Infrared spectroscopic study of the deliquescence and efflorescence of ammo-

AMTD
7, 1393–1455, 2014

nium sulfate aerosol as a function of temperature, J. Geophys. Res., 104, 21317–21326, 1999.
Pan, X. L., Yan, P., Tang, J., Ma, J. Z., Wang, Z. F., Gbaguidi, A., and Sun, Y. L.: Observational study of influence of aerosol hygroscopic growth on scattering coefficient over rural area near Beijing mega-city, Atmos. Chem. Phys., 9, 7519–7530, doi:10.5194/acp-9-7519-2009, 2009.
Poore, K. D., Wang, J. H., and Rossow, W. B.: Cloud layer thicknesses from a Combination of surface and upper-air obversions, Climate, 8, 550–568, 1995.
Randriamiarisoa, H., Chazette, P., Couvert, P., Sanak, J., and Mégie, G.: Relative humidity impact on aerosol parameters in a Paris suburban area, Atmos. Chem. Phys., 6, 1389–1407, doi:10.5194/acp-6-1389-2006, 2006.
Rogers, R. M., McCann, K., and Hoff, R. M.: Quantifying the Effect of Humidity on Aerosol Scattering with a Raman Lidar, 14th Joint Conference on the Applications of Air Pollution Meteorology with the Air and Waste Management Assoc., 2006.
Rosen, J. M., Pinnick, R. G., and Garvey, D. M.: Measurement of the extinction-to-backscatter for near-surface aerosols, J. Geophys. Res., 102, 6017–6024, 1997.
Ross, J. L., Hobbs, P. V., and Holben, B.: Radiative characteristics of regional hazes dominated by smoke from biomass burning in Brazil: closure tests and direct radiative forcing, J. Geophys. Res., 103, 31925–31941, 1998.
Salemink, H., Schotanus, P., and Bergwerff, J. B: Quantitative lidar at 532 nm for vertical extinction profiles in the lidar solution, Appl. Phys., 34B, 187–189, 1984.
Sassen, K.: The polarization lidar technique for cloud research: a review and current assessment, B. Am. Meteorol. Soc., 72, 1848–1866, 1991.
Sivakumar, V., Tesfaye, M., Alemu, W., Moema, D., Sharma, A., Bollig, C., and Mengistu, G.: CSIR South Africa mobile LIDAR – first scientific results: comparison with satellite, sun photometer and model simulations, S. Afr. J. Sci., 105, 449–455, 2009.
Skamarock, W. C.: Evaluating mesoscale NWP models using kinetic energy spectra, Mon. Weather Rev., 132, 3019–3032, 2004.
Spinhirne, J. D., Chudamani, S., Cabanaugh, J. F., and Bufton, J. L.: Aerosol and cloud backscatter at 1.06, 1.54, and 0.53 µm by airborne hard-target-calibrated Nd:YAG/methane Raman lidar, Appl. Optics, 36, 3475–3489, 1997.
Stoffelen, A., Pailleux, J., Källén, E., Vaughan, J. M., Isaksen, L., Flamant, P., Wergen, W., Andersson, E., Schyberg, H., Culoma, A., Meynart, M., Endemann, M., and Ingmann, P.:

AMTD
7, 1393–1455, 2014

The atmospheric dynamics mission for global wind measurement, B. Am. Meteorol. Soc., 86, 73–87, 2005.
Stoffelen, A., Marseille, G. J., Bouttier, F., Vasiljevic, D., de Haan, S., and Cardinali, C.: ADM-Aeolus doppler wind lidar observing system simulation experiment, Q. J. Roy. Meteor. Soc., 132, 1927–1947, doi:10.1256/qj.05.83, 2006.
Tan, D. G. H., Andersson, E., Fisher, M., and Isaksen, L.: Observing system impact assessment using a data assimilation ensemble technique: application to the ADM-Aeolus wind profiling mission, Q. J. Roy. Meteorol. Soc., 133, 381–390, 2007.
Tan, D. G. H., Andersson, E., Kloe, J. D., Marseille, G. J., Stoffelen, A., Poli, P., Denneulin, M. L., Dabas, A., Huber, D., Reitebuch, O., Flamant, P., Rille, O. L., and Nett, H.: The ADM-Aeolus wind retrieval algorithms, Tellus A, 60, 191–205, 2008a.
Tan, D. G. H., Andersson, E., Kloe, J. D, Marseille, G. J., Stoffelen, A., Poli, P., Dabas, A., Huber, D., Reitebuch, O., Flamant, P., Straume, A. G.,Rille, O. L., and Nett, H.: ADM-Aeolus Wind Retrieval Algorithms for NWP, 9th International Winds Workshop (9IWW), Annapolis, Maryland, USA, NOAA/NESDIS/EUMETSAT/CIMSS, 2008b.
Tang, I. N.: Chemical and size effects of hygroscopic aerosols on light scattering coefficients, J. Geophys. Res., 101, 19245–19250, 1996.
Tang, I. N. and Munkelwitz, H. R.: Composition and temperature dependence of the deliquescence properties of hygroscopic aerosols, Atmos. Environ., 27A, 467–473, 1993.
Vaisala: Vaisala RS92 Number One in WMO Intercomparison, available at: http://www.vaisala.com/VaisalaDocuments/VaisalaNewsArticles/VN186/vn186_04_vaisala-rs92-number-one-in-wmo-intercomparison.pdf (last access: 10 February 2014), 2011.
Vaughan, J. M.: Scattering in the atmosphere, in: Scattering and Inverse Scattering in Pure and Applied Science, edited by: Pike, E. R. and Sabatier, P. C., Academic Press, San Diego, 2002.
Vaughan, J. M., Geddes, N. J., Flamant, P. H., and Flesia, C.: Establishment of a Backscatter Coefficient and Atmospheric Database, ESA contract 12510/97/NL/RE, 110 pp., 1998.
Vaughan, M. A., Powell, K. A., Winker, D. M., and Hostetler, C. A.: Fully automated detection of cloud and aerosol Layers in the CALIPSO lidar measurements, J. Atmos. Ocean. Tech., 26, 2034–2050, 2009.
Waggoner, A. P., Ahlquist, N. C., and Charlson, R. J.: Measurement of the aerosol total scatter-backscatter ratio, Appl. Optics, 11, 2886–2889, 1972.

AMTD
7, 1393–1455, 2014

Wang, J. H. and Rossow, W. B.: Determinnation of cloud vertical structure from upper-air observations, J. Appl. Meteorol., 34, 2243–2258, 1995.

Winker, D. M.: The CALIPSO Mission and Initial Observations of Aerosols and Clouds from CALIOP, Proc. SPIE, 6409, 3 pp., 2006.

Zhang, J. Q., Chen, H. B., Li, Z. Q., Fan, X. H., Peng, L., Yu, Y., and Cribb, M.: Analysis of cloud layer structure in Shouxian, China using RS92 radiosonde aided by 95 GHz cloud radar, J. Geophys. Res., 115, D00K30, doi:10.1029/2010JD014030, 2010.

AMTD

7, 1393–1455, 2014

Table 1. Mean bias and variance for Mie and Rayleigh channel wind errors for a 1000 m vertical bin including a very thin cloud layer with one-way cloud transmission τ_c. A constant wind-shear of 0.004 s^{-1} over the bin is taken. The table values correspond to 3 different values for the one-way cloud transmission. X means no wind retrieval.

τ_c = 1/0.9/0	Mie channel		Rayleigh channel	
bias (ms^{-1})	X/0/0	Eq. (5)	0/0.1/1	Eq. (10)
variance ($m^2\,s^{-2}$)	X/1.33/1.33	Eq. (6)	0/0.004/0.33	Eq. (11)

AMTD
7, 1393–1455, 2014

Table 2. Height-resolving RH threshold profiles (from Zhang et al., 2010), see also Fig. 3.

Altitude Range	Height-Resolving RH Thresholds min-RH	max-RH	inter-RH
0–2 km	92–90 %	95–93 %	84–82 %
2–6 km	90–88 %	93–90 %	82–78 %
6–12 km	88–75 %	90–80 %	78–70 %
>12 km	75 %	80 %	70 %

AMTD
7, 1393–1455, 2014

Table 3. Typical values of backscatter (2nd column) and extinction (3rd column) for various cloud types (1st column) in the UV, visible and near-infraread part of the electromagnetic spectrum. The backscatter and extinction values are extracted from (Vaughan, 2002). FW cumulus means fair weather cumulus, PSC means polar stratospheric cloud.

Cloud type	β_C ($m^{-1}\,sr^{-1}$)	α_C (m^{-1})	Altitude range (km)
FW cumulus	6.0×10^{-4}	1.2×10^{-2}	2–4
Stratus	5.0×10^{-3}	9.0×10^{-2}	0.2–2
Alto-Stratus	1.0×10^{-3}	1.8×10^{-2}	2–6
Cumulo-Nimbus	1.0×10^{-2}	1.8×10^{-1}	2–16
Cirrus	1.4×10^{-5}	2.0×10^{-4}	5–16
PSC	3.0×10^{-7}	6×10^{-6}	16–30

AMTD
7, 1393–1455, 2014

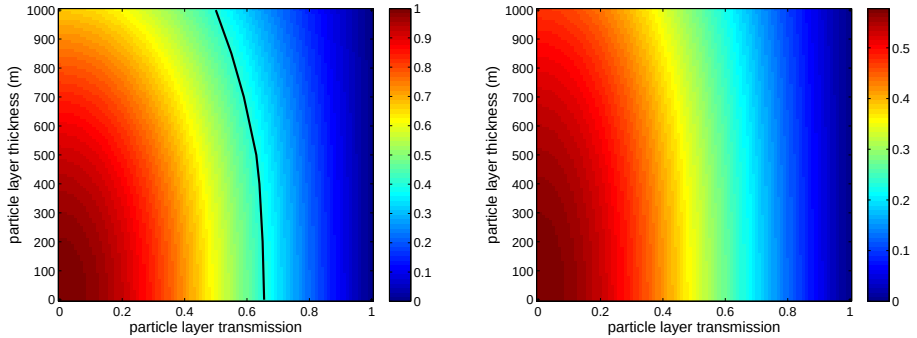

Fig. 1. Rayleigh wind error bias (ms^{-1}), Eq. (15), (left) and standard deviation (ms^{-1}), square root of Eq. (16), (right) as a function of the one-way transmission of the particle layer, τ_c, and particle layer thickness δz (m). The measurement bin size l is set at 1000 m, the wind-shear, α, is taken constant over the bin with a value of 0.004 s^{-1}. The black solid line in the left panel figure denotes the Aeolus mission wind error bias requirement of 0.4 ms^{-1}.

AMTD
7, 1393–1455, 2014

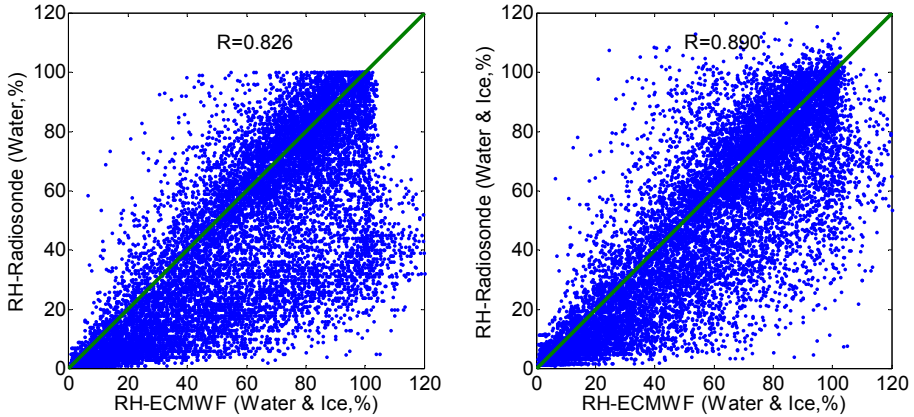

Fig. 2. Relative humidity (RH) over De Bilt for the year 2007 as obtained from radiosondes (y axis) and the ECMWF model (x axis). The intercomparison includes all attitudes from the surface up to the radiosonde altitude of about 20 km. The left panel shows the intercomparison based on measured liquid water only, yielding a correlation value of 0.826. The right panel shows the intercomparison after recalculation to two phases (right) yielding a correlation value of 0.890. See the text for details.

AMTD
7, 1393–1455, 2014


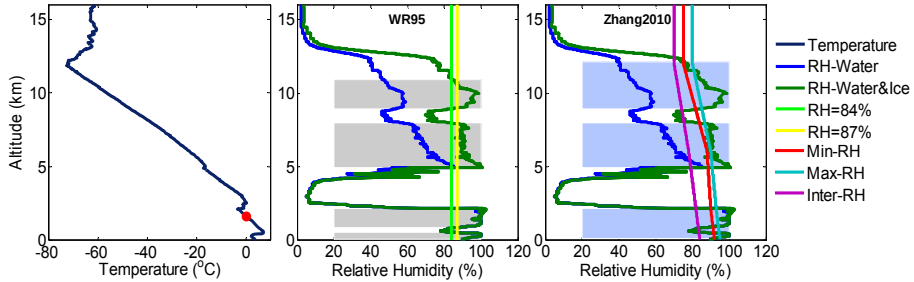

Fig. 3. Cloud layer detection by the WR95 and Zhang2010 method applied to the radiosonde launched in De Bilt on 27 December 2007 12:00 UTC. The left panel shows the temperature profile, the red point marking 0 °C. The middle and right panel are cloud layers detected by WR95 and Zhang2010, respectively: the blue line represents RH with respect to water, the dark green line represents RH with respect to ice for levels with temperatures below 0 °C, the green and yellow lines represent the constant minimum and maximum RH thresholds of 84 % and 87 % reported in WR95. The red, purple, and cyan lines represent min-RH, inter-RH and max-RH thresholds as a function of altitude, respectively, see Table 2.

AMTD
7, 1393–1455, 2014

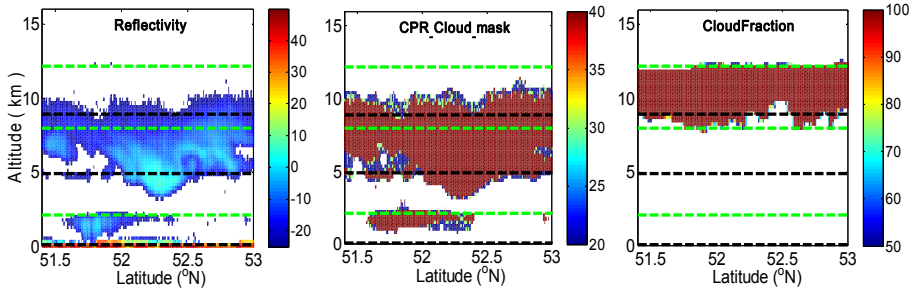

Fig. 4. Cloud layer detection from CloudSat/CALIPSO on 27 December 2007. The nearest distance of the CALIPSO overpass to De Bilt is 36 km. The local overpass time is 12:38 UTC Reflectivity (left) and CPR cloud mask (middle) are obtained from the 2B-GEOPROF data and cloud fraction (right) is obtained from the 2B-GEOPROF-Lidar data. The green dotted line and black dotted line are the corresponding cloud top and base determined by Zhang2010 respectively, see Fig. 3.

AMTD
7, 1393–1455, 2014

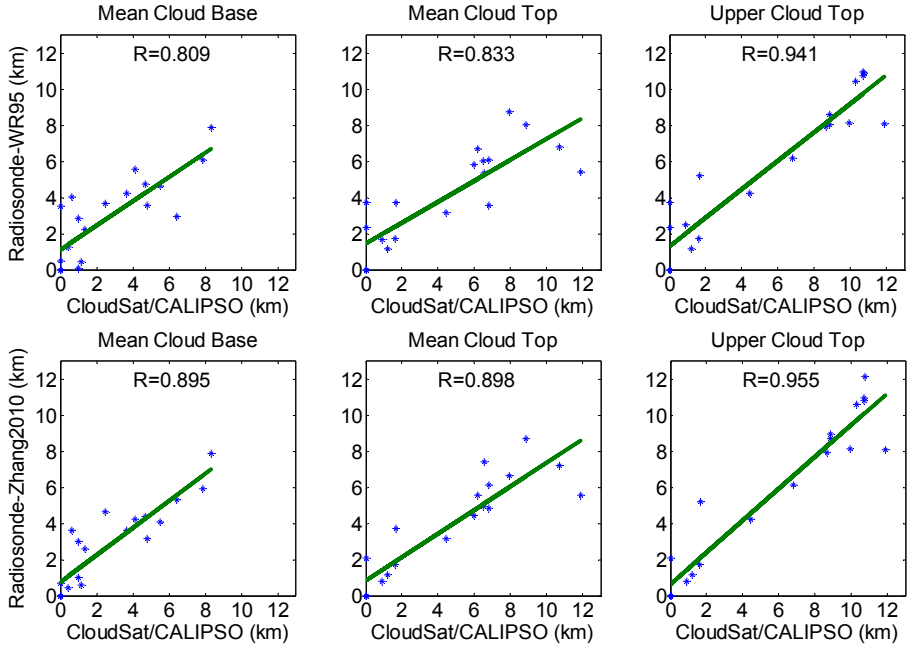

Fig. 5. Comparison of cloud parameters mean cloud base (left), mean cloud top (middle) and upper cloud top (right) between CloudSat/CALIPSO and radiosonde data processed by WR95 (upper row) and by Zhang2010 (bottom row). *R* denotes the correlation value between both datasets.

AMTD
7, 1393–1455, 2014

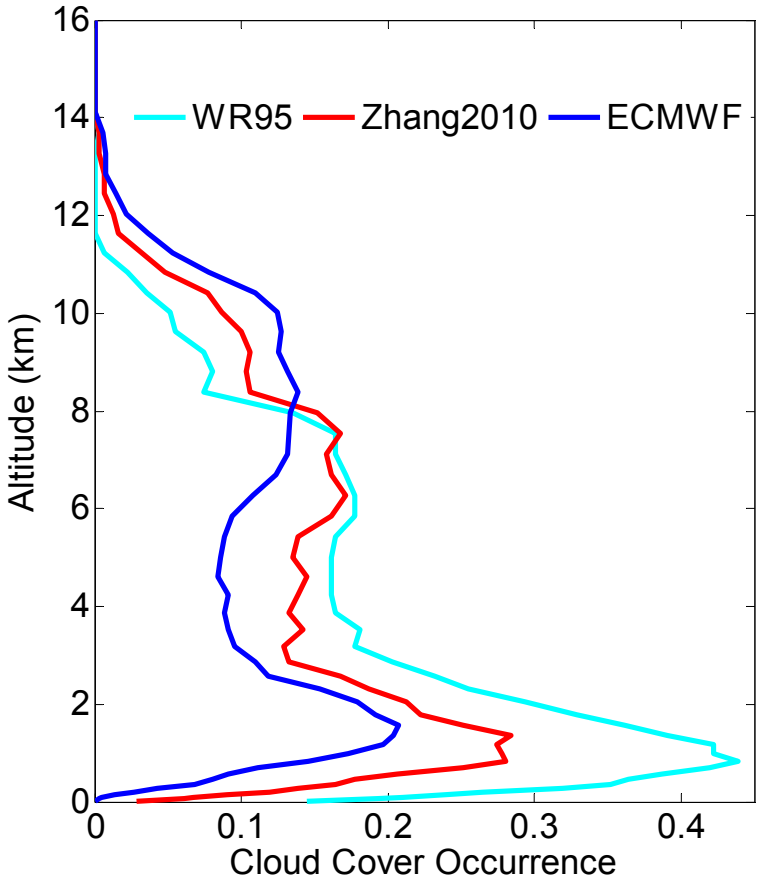

Fig. 6. Mean cloud cover over de Bilt for the 1 yr period 2007. The blue/red/cyan line represents ECMWF/Zhang2010/WR95.

AMTD
7, 1393–1455, 2014

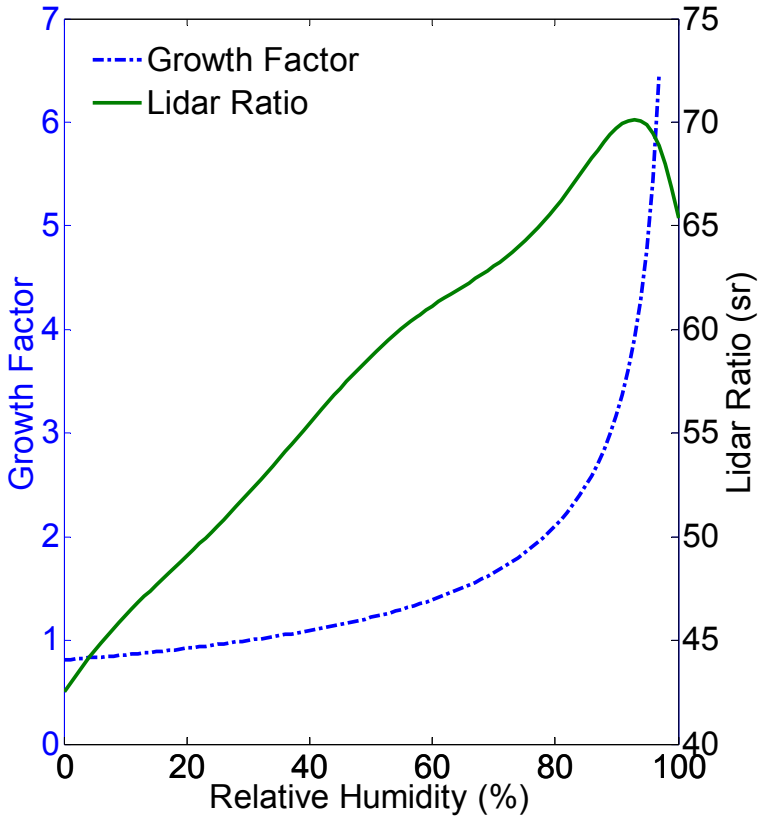

Fig. 7. Simulations of growth factor (blue), Eq. (31), and lidar ratio (sr) (green), Eq. (27), as a function of RH.

AMTD
7, 1393–1455, 2014

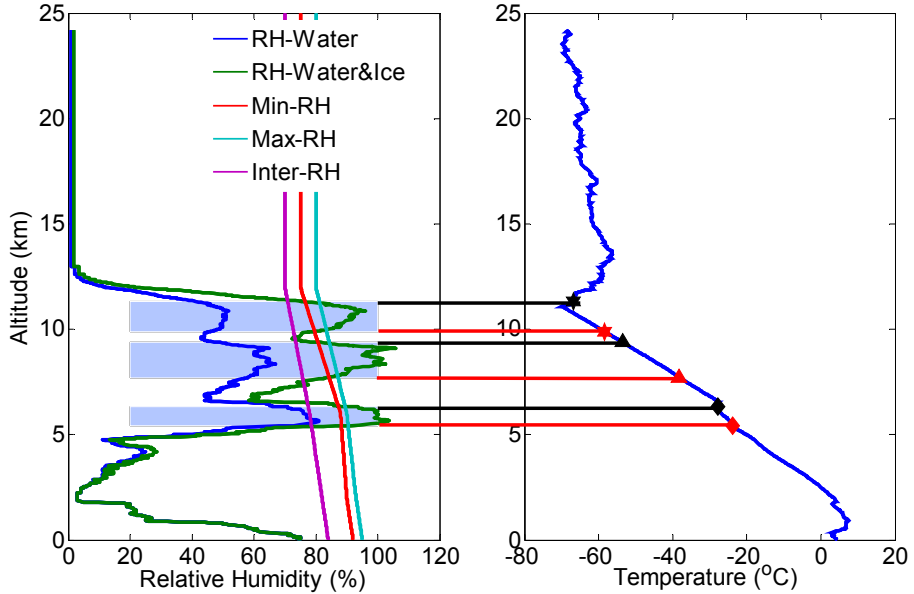

Fig. 8. Relative humidity (%) (left) and temperature (°C) (right) with altitude (km) from the radiosonde launched in De Bilt on 25 December 2007 12:00 UTC. Three cloud layers were detected by the Zhang2010 method. Diamonds, triangles and asterisks correspond to the location of the lower, middle and upper cloud respectively with cloud base in red and cloud top in black.

AMTD
7, 1393–1455, 2014

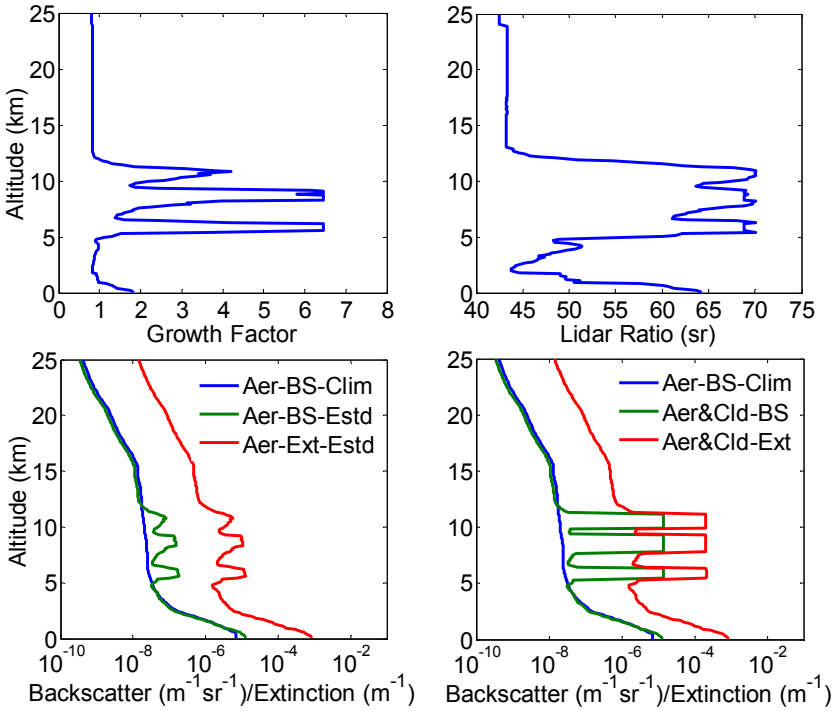

Fig. 9. Aerosol growth factors (upper left) and lidar ratio (upper right) obtained from the radiosonde data of Fig. 8. Martime aerosol is assumed over De Bilt, giving aerosol backscatter and extinction in the lower left panel. Total backscatter and extinction from aerosol and clouds is shown in the lower right panel. Blue, dark green and red lines in the lower left panel represent the climatological aerosol backscatter coefficient ($m^{-1}\,sr^{-1}$), estimated aerosol backscatter coefficient ($m^{-1}\,sr^{-1}$), including the relative humidity growth factor, and estimated aerosol extinction coefficient (m^{-1}), respectively. In the lower right panel, the dark green and red lines represent the estimated combined aerosol and cloud backscatter coefficient ($m^{-1}\,sr^{-1}$), and estimated combined aerosol and cloud extinction coefficient (m^{-1}), respectively.

AMTD
7, 1393–1455, 2014

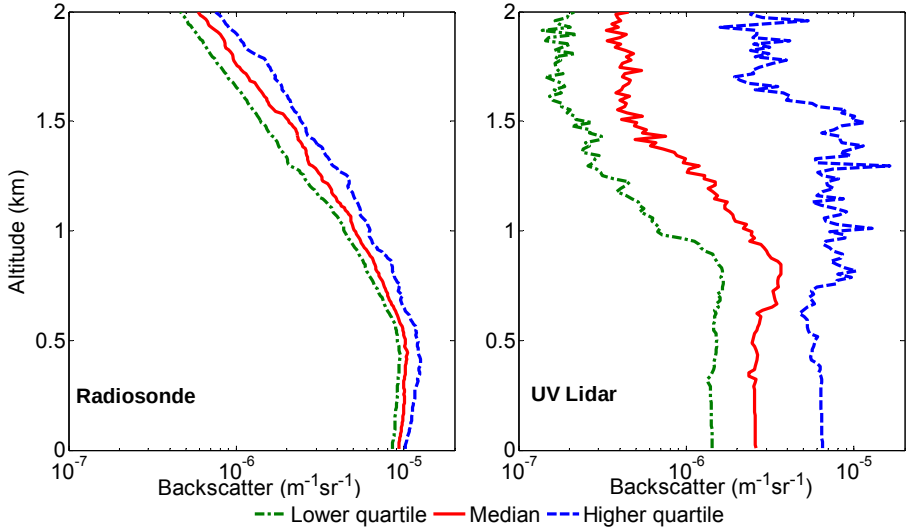

Fig. 10. Aerosol backscatter coefficient ($m^{-1}\,sr^{-1}$) statistics at 355 nm wavelength as obtained from radiosondes (left) and the UV lidar (right). Red/green/blue lines denote the median/lower quartile/higher quartile percentiles respectively.

AMTD
7, 1393–1455, 2014

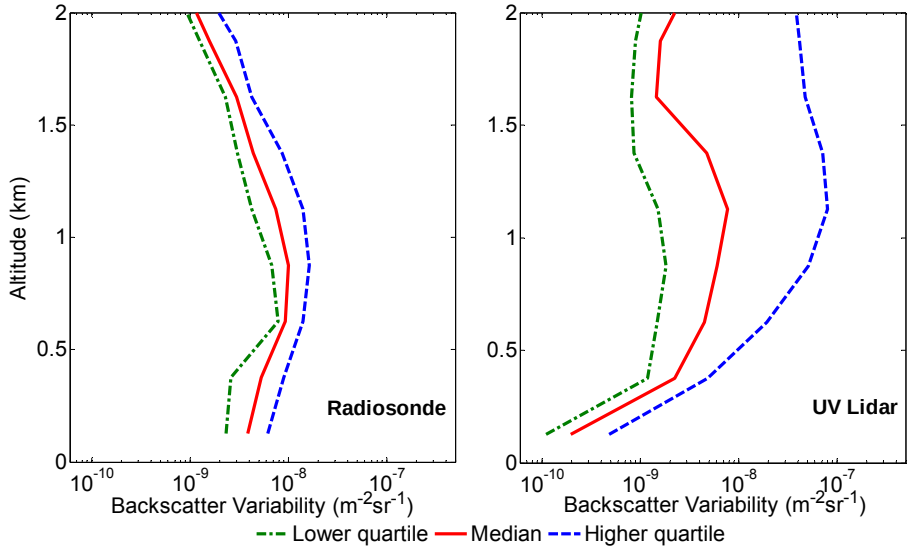

Fig. 11. Same as Fig. 10 but now for the aerosol backscatter coefficient variability ($m^{-2}\,sr^{-1}$).

AMTD
7, 1393–1455, 2014

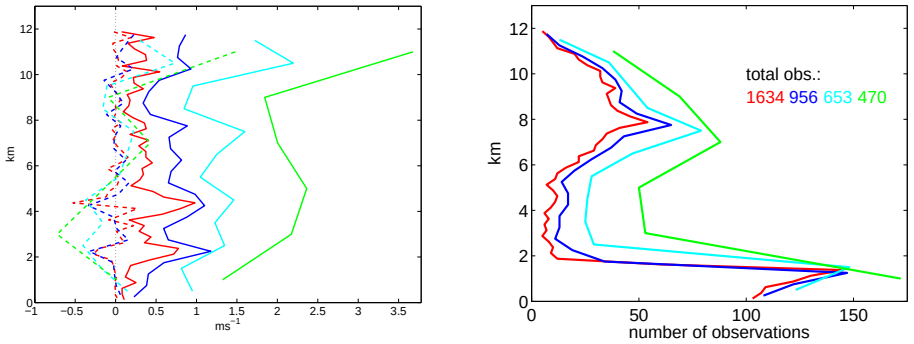

Fig. 12. Aeolus Mie wind error statistics (left panel) and coverage (right panel) as a function of bin size: 250 m (red), 500 m (blue), 1000 m (cyan) and 2000 m (green). Dashed and solid lines in the left panel correspond to the error bias and standard deviation respectively. The statistics are based on 309 radiosondes launched at 12:00 UTC in De Bilt in 2007. The total number of Mie winds as a function of bin size is given in the legend of the right panel.

AMTD
7, 1393–1455, 2014

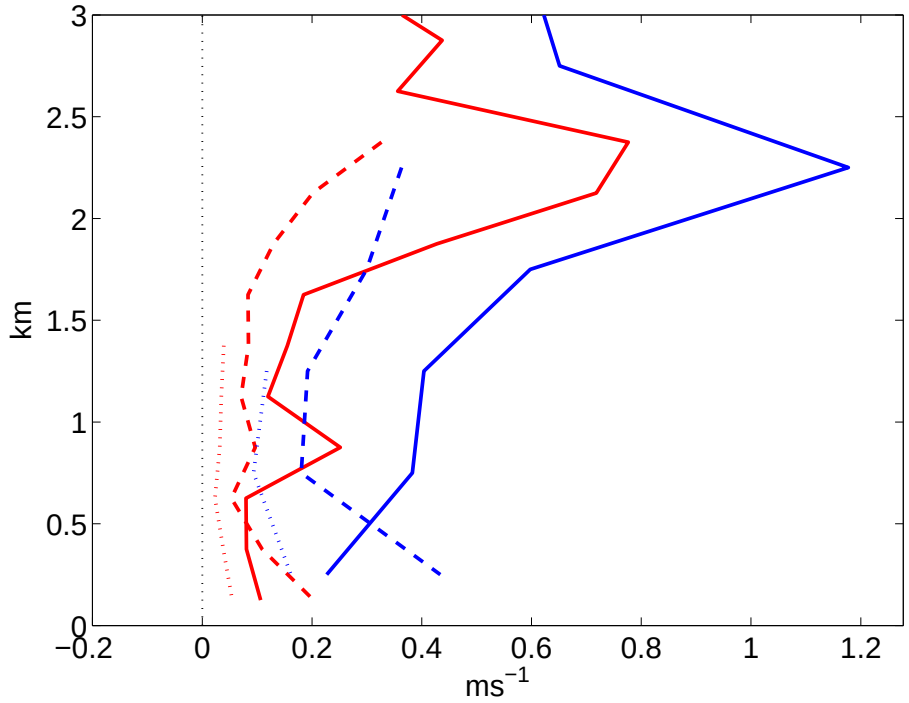

Fig. 13. Mie wind error standard deviation for 250 m (red) and 500 m (blue) bin size for three different particle regimes: (i) a climatological smooth aerosol reference model atmosphere (dotted), no clouds, (ii) the parameterization of Eq. (25) (dashed), no clouds and (iii) from the radiosonde database, i.e., Eq. (25) for aerosol backscatter, including clouds (solid). The solid lines are identical to Fig. 12.

AMTD
7, 1393–1455, 2014

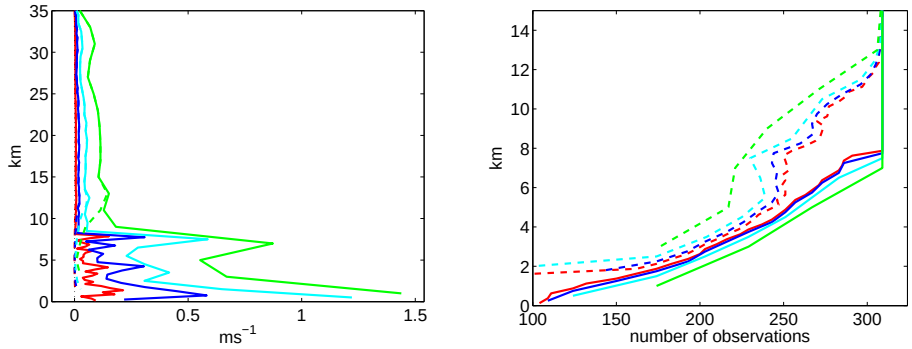

Fig. 14. Aeolus Rayleigh wind error standard deviation (left panel) and coverage (right panel) as a function of bin size: 250 m (red), 500 m (blue), 1000 m (cyan) and 2000 m (green). Dashed and solid lines correspond to processing with and without taking into account signal classification respectively, see the text for details. The statistics are based on 309 radiosondes launched at 12:00 UTC in De Bilt in 2007. The *y* axis of the right panel is cut at 15 km, but winds from all 309 launches were obtained up to 35 km.

AMTD
7, 1393–1455, 2014